A Field Study of the Wind Generation of Ocean Waves[1]

Russell L. Snyder

Institute of Marine Science
University of Miami
Miami, Florida

Charles S. Cox

Scripps Institution of Oceanography
University of California at San Diego
La Jolla, California

ABSTRACT

This paper describes a series of field experiments that provide growth curves and wind histories for waves of wave length 17 m. In each of 29 runs of from 1 to 4 hours, a directional wave recorder with an effective beam width of 20 degrees was towed downwind at the group velocity of these waves starting from a windward shore. The observed growth curves are initially consistent with a linear form of Hasselmann's equation (1960), which, in the moving reference frame, states that $(d/dt)\,F = \alpha + \beta F$, where F is the spectral intensity of the 17-m component, and α and β are determined by the local wind. At spectral intensities greater than 30% of the equilibrium value, the growth rate diminishes because of nonlinear effects. α is of order 10^{-4} cm^2 and is positively correlated with wind speed (measured 6.1 m above the surface) in the range 10–20 knots or 5–10 m sec^{-1}. β is approximately linear in wind speed over this same range, the best linear fit having a slope of $(0.20 \pm 0.03) \times 10^{-3}$ sec^{-1} knots^{-1} or $(0.40 \pm 0.06) \times 10^{-3}$ m^{-1} and an intercept of (7.7 ± 1.0) knots or (3.9 ± 0.5) m sec^{-1}. This fit is approximated by the rather simple relationship $\beta = s\,(\boldsymbol{k}_0 \cdot \boldsymbol{W} - \omega_0)$, where s is the ratio between the density of air and water, $\boldsymbol{k}_0$ and ω_0 are the propagation vector and frequency of the 17-m component, and $\boldsymbol{W}$ is the wind velocity measured one wave length above the water surface. The growth rate for wind speeds below the phase speed of 10 knots is only imperfectly known since, under these conditions, F could not be recovered from the towed wave record.

The dominant growth mechanism is associated with the instability term βF, α being significant only near the upwind edge of the fetch. It is noteworthy that the observed values of β are almost an order of magnitude larger than those predicted by the theories of Jeffreys (1925) and Miles (1957). The observed values of α are compared with the theory of Phillips (1957), using Priestley's (1965) measurements of the longitudinal, lateral, and diagonal correlations of atmospheric pressure fluctuations over land. Assuming the atmospheric

1. Contribution No. 681 from the Institute of Marine Science, University of Miami.
Contribution from the Scripps Institution of Oceanography, New Series.
Accepted for publication and submitted to press 12 February 1966.

turbulence present during Priestley's measurements to be comparable to that present during ours, this comparison confirms Phillips' theory, at least for wind speeds in the neighborhood of the phase speed. Extrapolation of Priestley's results to higher wind speeds suggests that Phillips' theory may account for the observed values of α for these wind speeds as well.

Comparison with measurements by Burling (1955) and Kinsman (1960) suggests a universal relationship between the fetch (in wave lengths) at which a wave component occupies the steep forward face of the spectrum and the wind speed (in multiples of the phase speed). This fetch is not in agreement with the assumption of Phillips and Katz (1961).

An estimate of the transfer of horizontal momentum by normal stress suggests that for a fully developed sea this transfer is large compared with the transfer by tangential stress.

INTRODUCTION

1.1. *Brief Summary of Theoretical Results.* Theories of the wind generation of ocean waves have generally involved one of two mechanisms: (i) surface instability, or (ii) random excitation by atmospheric pressure fluctuations. Examples of (i) are the theories of Kelvin (1910) and Helmholtz (1868), Jeffreys (1925), and Miles (1957), and of (ii) the theories of Eckart (1953) and Phillips (1957).

The instability theories depend upon the coupling between surface waves and coherent wave-induced atmospheric pressure fluctuations. Characteristically, they predict an exponential increase with time or fetch in the energy of a particular wave component. In the Kelvin-Helmholtz theory the wave-induced perturbation of atmospheric pressure is exactly 180 degrees out of phase with the surface elevation. Instability results when the Bernoulli suction on a wave crest exceeds the restoring forces. Because the wind speeds necessary to produce Kelvin-Helmholtz instability in gravity waves are far in excess of those normally encountered at sea, it is unlikely that this form of instability can be very important as a generating mechanism. A more efficient coupling of surface waves and the wave-induced perturbation of atmospheric pressure results when there is a component of this perturbation that lags the surface elevation by 90 degrees. Such is the case in the sheltering theory of Jeffreys and in the shear-flow theory of Miles. The former postulates a separation of the flow in the lee of a wave crest. According to Jeffreys this separation gives rise to a fluctuation of atmospheric pressure that is proportional to the wave slope and, in analogy to the case of turbulent flow around solid objects, to the square of the difference between the wind speed W and the phase speed C. Unlike Jeffreys, Miles has neglected any direct interaction between atmospheric turbulence and surface waves, but he has allowed for a velocity shear in the mean air flow. The resulting instability depends upon the ratio of the curvature of the wind profile to its slope at a distance above the water surface for which $W = C$.

The theories of Eckart and Phillips are uncoupled in the sense that the wave-induced perturbation of atmospheric pressure is ignored. In Phillips' theory the ocean is viewed as a resonant system excited by incoherent turbulent

atmospheric pressure fluctuations. The theory predicts a linear increase with time or fetch in the energy of a particular wave component. An important aspect of the theory is the prediction that this increase should be particularly large for wave components satisfying the relation

$$\boldsymbol{k} \cdot \boldsymbol{W} - \omega(k) = 0 ,$$

where $\boldsymbol{k}$ is the propagation vector of the component, $\omega(k)$ the corresponding angular frequency, and $\boldsymbol{W}$ the mean wind velocity measured an appropriate height above the water surface. It has been generally doubted that Phillips' mechanism can account for the major growth of the spectrum, since the incoherent pressure fluctuations are probably too small, but the mechanism is considered to be important in initially raising the spectrum to a point where an instability mechanism can become effective.

Hasselmann (1960) has proposed a general equation that includes as special cases the theories of Jeffreys, Miles, and Phillips, while also allowing for nonlinear interactions. In the linear range, Hasselmann's equation reads

$$\frac{\partial}{\partial t} F(\boldsymbol{x},t,\boldsymbol{k}) + \boldsymbol{V}(\boldsymbol{k}) \cdot \nabla F(\boldsymbol{x},t,\boldsymbol{k}) = \alpha(\boldsymbol{x},t,\boldsymbol{k}) + \beta(\boldsymbol{x},t,\boldsymbol{k}) F(\boldsymbol{x},t,\boldsymbol{k}) , \qquad (1)$$

where $F(\boldsymbol{x}, t, \boldsymbol{k})$ is the spectral intensity of the $\boldsymbol{k}$ component at the point $\boldsymbol{x}$ at time t, $\boldsymbol{V}(\boldsymbol{k})$ is the group velocity of this component,

$$\boldsymbol{V}(\boldsymbol{k}) \equiv \nabla_{\boldsymbol{k}} \omega(k) ,$$

and the coefficients $\alpha(\boldsymbol{x},t,\boldsymbol{k})$ and $\beta(\boldsymbol{x},t,\boldsymbol{k})$ are functions of the local wind. The term α represents the input of energy to the $\boldsymbol{k}$ component from incoherent atmospheric pressure fluctuations, while the term βF represents the input from coherent fluctuations 90 degrees out of phase with the surface elevation. A systematic derivation of the above equation from first principles has been given by Snyder (1965).

THE EXPERIMENT

2.1. *Approach.* This paper describes a series of field experiments designed to follow the evolution of a single wave component under the action of the wind. A wave recorder was towed downwind at constant velocity starting from a windward shore, and the wind velocity was monitored simultaneously. This procedure provides a growth curve and complete wind history for that component having a group velocity equal to the towing velocity.

The success of the method depends largely upon two circumstances. One of these is the simplification of Hasselmann's equation for that component having a group velocity equal to the towing velocity. The other is the singular

nature of the spectral transformation, which allows us to estimate the spectral intensity of this same component from the spectrum of the towed wave record.

Let $\boldsymbol{k}_0$ be defined by the relation

$$\boldsymbol{V}(\boldsymbol{k}_0) = \boldsymbol{U},$$

where $\boldsymbol{u}$ is the towing velocity, and let

$$F(t, \boldsymbol{k}) = F(\boldsymbol{U}t, t, \boldsymbol{k}),$$

$$\alpha(t, \boldsymbol{k}) = \alpha(\boldsymbol{U}t, t, \boldsymbol{k}),$$

and

$$\beta(t, \boldsymbol{k}) = \beta(\boldsymbol{U}t, t, \boldsymbol{k}).$$

The left-hand quantities are the values of F, α, and β as observed from a reference frame moving with the velocity $\boldsymbol{U}$. It follows from (1) that

$$\frac{\partial}{\partial t} F(t, \boldsymbol{k}_0) = \alpha(t, \boldsymbol{k}_0) + \beta(t, \boldsymbol{k}_0) F(t, \boldsymbol{k}_0). \tag{2}$$

This paper is concerned with an attempt to represent the coefficients α and β as functions of the mean wind velocity $\boldsymbol{W}(\boldsymbol{x}, t)$ measured at some level above the ocean surface. More precisely, we attempt to describe the initial generation of 17-m wind waves by means of (2), where α and β are of the form

$$\alpha(t, \boldsymbol{k}_0) = \alpha(W_1(t)),$$

and

$$\beta(t, \boldsymbol{k}_0) = \beta(W_1(t)),$$

where

$$W_1(t) \equiv \frac{\boldsymbol{k}_0}{k_0} \cdot \boldsymbol{W}(\boldsymbol{U}t, t).$$

Eq. (2) becomes

$$\frac{\partial}{\partial t} F(t, \boldsymbol{k}_0) = \alpha(W_1(t)) + \beta(W_1(t)) F(t, \boldsymbol{k}_0). \tag{3}$$

Eq. (3) provides the justification for the experimental procedure. The towed wave record allows a determination of $F(t, \boldsymbol{k}_0)$ while the anemometer gives $W_1(t)$. A best fit for $\alpha(W_1)$ and $\beta(W_1)$ is determined by a least-squares analysis and (1) evaluated from the resulting fit. The best fit $\alpha(W_1)$ and $\beta(W_1)$ are then compared with theoretical predictions.

2.2. *Experimental Details.* A schematic representation of the experimental arrangement is given in Fig. 1. An end-fire array of four 1.8 m × 1.2 m catamaran rafts was towed at a distance of 135 m. The array was tuned to

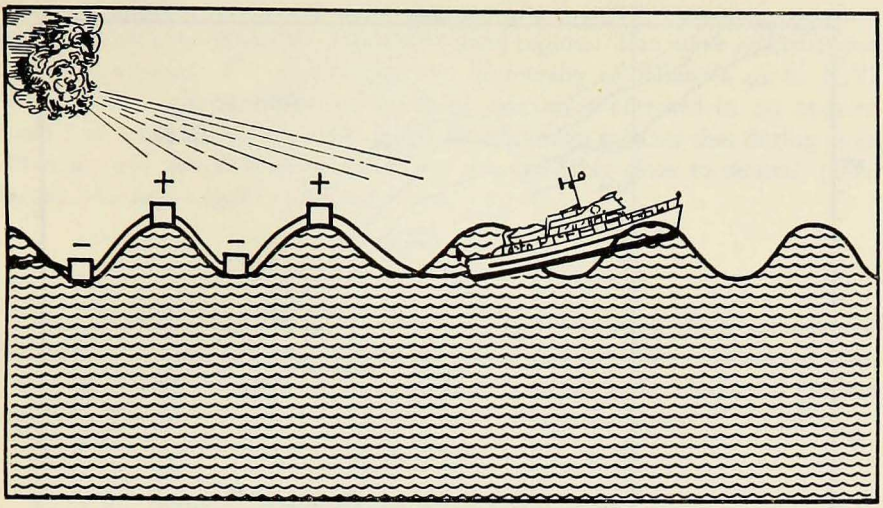

Figure 1. Schematic diagram of the experimental arrangement.

waves having a wave length of 17 m, the spacing between the rafts being 8.5 m or half a critical wave length. Two 45-m polypropylene draglines were trailed from the last raft to prevent the rafts from surfing.

Housed in a waterproof box on each raft was a gymbal-mounted vertical accelerometer.[2] The signals from the four accelerometers were alternately added and subtracted, and the resulting signal was returned to the towing vessel through the tow cable. Here the signal was low-pass filtered, integrated, converted to a frequency-modulated signal, and recorded on magnetic tape. A timing pulse was recorded on a second channel of the tape every 0.25 sec. Readout of the data was accomplished in the laboratory by means of an electronic counter and paper tape punch.[3]

The mean wind velocity was monitored by an aerovane mounted 6.1 m above the water surface; its installation is pictured schematically in Fig. 1.

The wave recorder was calibrated (i) electronically, using a low-frequency signal generator and accepting the factory calibration of the accelerometers, and (ii) mechanically, using a device (built by William Van Dorn) that simulates wave motions with periods of from 1 to 40 sec. The wind recorder was calibrated by mounting the aerovane above the cab of a truck and driving back and forth along a measured mile at various speeds. The geometry of this calibration, though far from ideal, simulates to some extent the geometry of the field experiments. The calibration of both recorders is considered accurate to about 3%.

2. Systron-Donner Model 4310.
3. The spectra computed from these data have units of counts squared (cts^2).

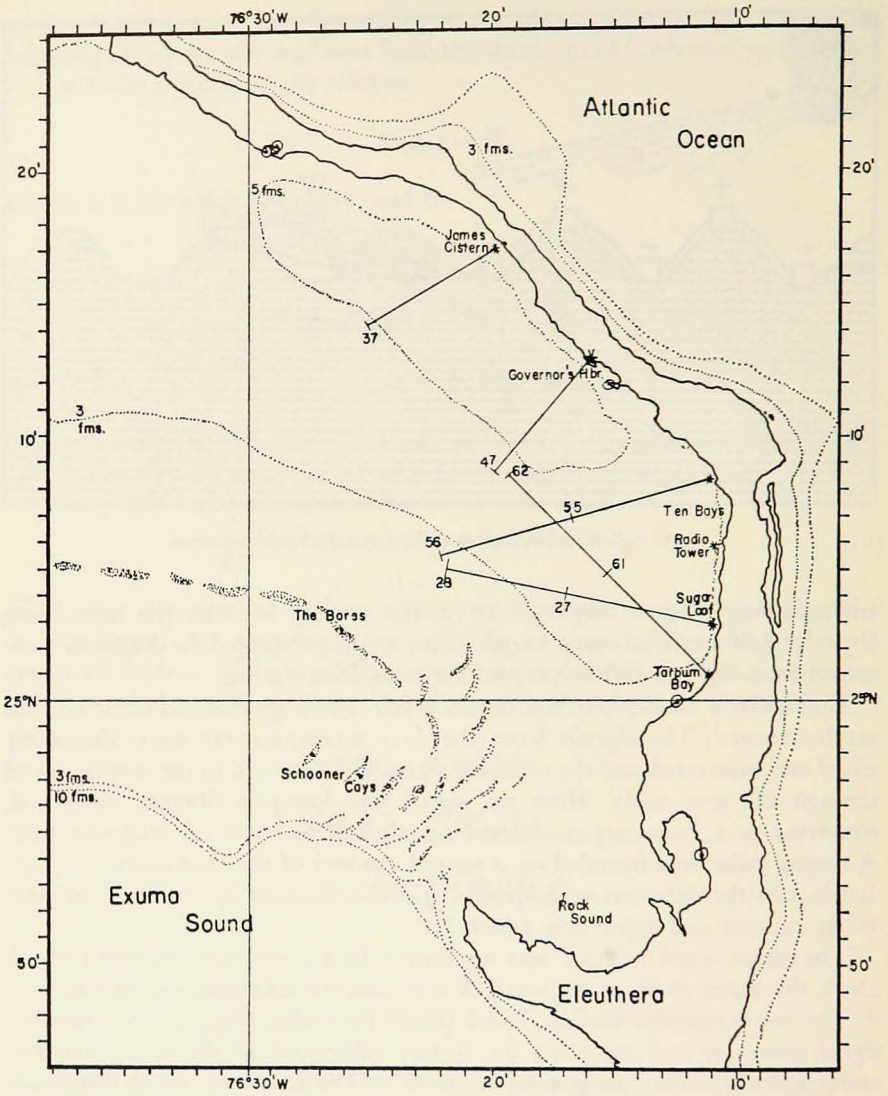

Figure 2. Chart of the area of the field experiments.

The principal means of monitoring the towing speed was a taffrail log. Secondary checks of position were provided by celestial navigation and by coastal bearings. The log was calibrated over a measured mile before and after the field experiments, and these calibrations agree to within 1%.

The field experiments were carried out during the spring of 1963 in the lee of Eleuthera Island in the Bahamas. A chart of the area, including the

tracks of several runs, is given in Fig. 2. The location combined excellent geometry with a reasonably dependable wind regime. The wave recorder was towed at a speed of 5 knots from the University of Miami's 42-ft. R.V. BUCCANEER. Approximately 51 hours of data were obtained in 29 runs of from 1 to 4 hours. Air-water temperature differences indicate that during most of these runs the atmospheric stability was probably close to neutral. (The largest observed negative difference was $-0.7°$C.)

ANALYSIS OF THE DATA

3.1. *The Frequency Mapping.* The relationship between the frequency and direction of a wave and its apparent frequency and direction as observed from a moving reference frame has been discussed in detail by St. Denis and Pierson (1953). A somewhat less-detailed presentation is given here.

We imagine a disturbance of the form

$$\zeta(\boldsymbol{x}, t) = \zeta_0 \cos(\boldsymbol{k} \cdot \boldsymbol{x} - \omega(k)t + \Phi).$$

The vertical displacement at the point $\boldsymbol{U}t$ is of the form

$$\zeta(\boldsymbol{U}t, t) = \zeta_0 \cos(\Omega(\boldsymbol{k})t - \Phi),$$

where the apparent frequency $\Omega(\boldsymbol{k})$ is given by

$$\Omega(\boldsymbol{k}) \equiv \omega(k) - \boldsymbol{k} \cdot \boldsymbol{U}. \tag{4}$$

Let $\boldsymbol{k}_0$ be the propagation vector of those waves having a group velocity $\boldsymbol{V}(\boldsymbol{k}_0)$ equal to $\boldsymbol{U}$. Then it can be shown that in deep water

$$\omega_0 \equiv \omega(k_0) = \frac{g}{2U},$$

and

$$\Omega_0 \equiv \Omega(\boldsymbol{k}_0) = \frac{g}{4U} = \frac{\omega_0}{2},$$

where g is the acceleration of gravity. In terms of ω and ϑ, (4) may be written

$$\Omega = \Omega(\omega, \vartheta) = \omega - \frac{\omega^2}{4\Omega_0} \cos\vartheta, \tag{5}$$

where

$$\cos\vartheta \equiv \frac{\boldsymbol{k} \cdot \boldsymbol{U}}{kU}.$$

Relation (5) is contoured for $\omega > 0$ in Fig. 3.

The inverse mapping, $\omega = \omega(\Omega, \vartheta)$, is nonunique. The nature of this nonuniqueness is clarified by an examination of Fig. 3. We note that for $|\vartheta| < \pi/2$ fixed and $0 < \Omega \cos\vartheta < \Omega_0$ there are, in general, two values of ω corresponding

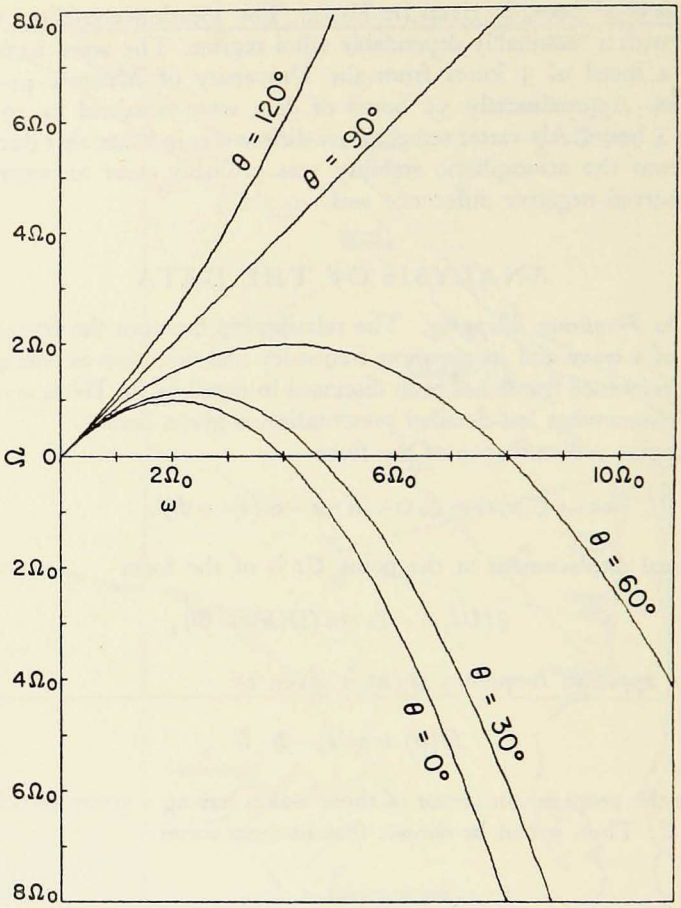

Figure 3. The frequency mapping. Note the compression for small ϑ of the apparent frequency $\Omega(\omega, \vartheta)$ near $\omega = \omega_0 = 2\,\Omega_0$.

to a given value of Ω and a third value corresponding to $-\Omega$. Because the spectral analysis does not distinguish between positive and negative frequencies, the resulting spectral transformation involves a sum of three integrals.

3.2. *The Spectral Transformation.* The transformation relating the spectrum $F(\boldsymbol{k})$ to the apparent spectrum (or spectrum of encounter) $E(\Omega)$ obtained from a towed wave record has been discussed by Cartwright (1961). For a more detailed exposition of the present discussion, the reader is referred to Snyder (1965).

We assume the recorded signal $f(t)$ to be a convolution of the surface elevation $\zeta(\boldsymbol{x}, t)$:

$$f(t) = \int_{-\infty}^{\infty} d^2x_1\, dt_1\, s(\mathbf{U}t - \mathbf{x}_1)\, r(t - t_1)\, \zeta(\mathbf{x}_1, t_1)\,.$$

It follows that

$$E(\Omega) = \frac{1}{2} R(\Omega) \int_{-\infty}^{\infty} d^2k\, S(\boldsymbol{k})\, F(\boldsymbol{k}) [\delta(\Omega - \Omega(\boldsymbol{k})) + \delta(\Omega + \Omega(\boldsymbol{k}))]\,, \tag{6}$$

where

$$R(\Omega) \equiv \left| \int_{-\infty}^{\infty} d\tau\, r(\tau) e^{-i\Omega\tau} \right|^2,$$

and

$$S(\boldsymbol{k}) \equiv \left| \int_{-\infty}^{\infty} d^2\xi\, s(\boldsymbol{\xi}) e^{-i\boldsymbol{k}\cdot\boldsymbol{\xi}} \right|^2;$$

$R(\Omega)$ is the temporal response of the wave recorder, and $S(\boldsymbol{k})$ is its spatial response. By changing the variables of integration and expanding the delta functions, we may write (6) in the form

$$\begin{aligned} E(\Omega) = {} & \frac{1}{2} R(\Omega) \int_{\vartheta_0(\Omega)}^{\pi} d\vartheta\, \frac{\Omega_0}{(\Omega_0^2 - \Omega\Omega_0 \cos\vartheta)^{1/2}} K(\omega_1(\Omega,\vartheta),\vartheta) + \\ & + \frac{1}{2} R(\Omega) \int_{\vartheta_0(\Omega)}^{\pi/2} d\vartheta\, \frac{\Omega_0}{(\Omega_0^2 - \Omega\Omega_0 \cos\vartheta)^{1/2}} K(\omega_2(\Omega,\vartheta),\vartheta) + \\ & + \frac{1}{2} R(\Omega) \int_{0}^{\pi/2} d\vartheta\, \frac{\Omega_0}{(\Omega_0^2 + \Omega\Omega_0 \cos\vartheta)^{1/2}} K(\omega_2(-\Omega,\vartheta),\vartheta)\,, \end{aligned} \tag{7}$$

where

$$\vartheta_0(\Omega) \equiv \cos^{-1}\left(\frac{\Omega_0}{\Omega}\right), \quad \Omega > \Omega_0\,,$$

$$\equiv 0\,, \quad \Omega \leqslant \Omega_0\,,$$

$$\omega_1(\Omega,\vartheta) \equiv \frac{2}{\cos\vartheta} [\Omega_0 - (\Omega_0^2 - \Omega\Omega_0 \cos\vartheta)^{1/2}]\,, \tag{8}$$

$$\omega_2(\Omega,\vartheta) \equiv \frac{2}{\cos\vartheta} [\Omega_0 + (\Omega_0^2 - \Omega\Omega_0 \cos\vartheta)^{1/2}]\,, \tag{9}$$

and

$$K(\omega,\vartheta) \equiv S(\omega,\vartheta) [F(\omega,\vartheta) + F(\omega,-\vartheta)]\,.$$

Here

$$S(\omega,\vartheta) \equiv S(\boldsymbol{k}(\omega,\vartheta))\,,$$

and

$$F(\omega,\vartheta) \equiv \frac{2\omega^3}{g^2} F(\boldsymbol{k}(\omega,\vartheta))\,.$$

In the derivation of (7) it has been assumed that $S(\omega,-\vartheta) = S(\omega,\vartheta)$.

Under the conditions of the experiment, relation (7) may be simplified by means of two approximations. The first of these depends upon the observation

that in a locally generated wind sea there is little energy associated with wave components traveling at angles of more than 90 degrees to the wind. As a result, the upper limit of the first integral on the right-hand side of (7) may be set equal to $\pi/2$. The second approximation depends primarily upon the form of $S(\omega, \vartheta)$. We note from (9) that $\omega_2(-\Omega, \vartheta) \geqslant 4\,\Omega_0$ for $\Omega > 0$ and $|\vartheta| < \pi/2$. Thus the third integral on the right-hand side of (7) involves only the high-frequency behavior of $S(\omega, \vartheta)$. Since the rafts were constructed with sufficient length and beam that their response to such high-frequency waves was small,

$$S(\omega, \vartheta) \cong 0\,, \quad \omega \geqslant 4\,\Omega_0\,; \tag{10}$$

and the integral may be neglected altogether. Even if there exists a range about $\omega = 4\,\Omega_0$, for which (10) is not satisfied, this integral will generally be small compared with the remaining integrals, provided $F(\omega, \vartheta)$ is peaked for some $\omega < 4\,\Omega_0$.

Making both approximations we obtain the relation

$$E(\Omega) = \frac{1}{2} R(\Omega) \int_{\vartheta_0(\Omega)}^{\pi/2} d\vartheta \frac{\Omega_0}{(\Omega_0^2 - \Omega\Omega_0 \cos\vartheta)^{1/2}}$$
$$[K(\omega_1(\Omega, \vartheta), \vartheta) + K(\omega_2(\Omega, \vartheta), \vartheta)]\,. \tag{11}$$

The singularity for $\boldsymbol{k} = \boldsymbol{k}_0$ is already evident in the integrand of (11). The nature of this singularity is clarified by considering the smoothed spectrum

$$G(\sigma) \equiv 2 \int_{\sigma - 2\sigma_0}^{\sigma + 2\sigma_0} d\Omega\, T(\sigma - \Omega)\, E(\Omega)\,. \tag{12}$$

$G(\sigma)$ is the spectrum estimated by a time-series analysis of the towed wave record, where $T(\omega)$ is the cosine transform of the corresponding lag window. $T(\omega)$ is assumed to be negligible outside some interval $(-2\,\sigma_0, 2\,\sigma_0)$. For a cosine taper (hanning), σ_0 is given by $\sigma_0 = \pi/l\,\Delta t$, where l is the number of lags and Δt is the data interval. Writing $G(\sigma)$ as a double integral, we have

$$G(\sigma) = \int_{\sigma - 2\sigma_0}^{\sigma + 2\sigma_0} d\Omega\, R(\Omega)\, T(\sigma - \Omega)$$
$$\int_{\vartheta_0(\Omega)}^{\pi/2} d\vartheta \frac{\Omega_0}{(\Omega_0^2 - \Omega\Omega_0 \cos\vartheta)^{1/2}} [K(\omega_1(\Omega, \vartheta), \vartheta) + K(\omega_2(\Omega, \vartheta), \vartheta)]. \tag{13}$$

The integrand of (13) is singular along the line $\cos\vartheta = \Omega_0/\Omega$. The singularity is particularly intense at the point $\cos\vartheta = \Omega_0/\Omega = 1$. Except at this point this singularity is integrable with respect to ϑ. It is thus clear that for $\sigma - 2\,\sigma_0 <$

$\Omega_0 < \sigma + 2\,\sigma_0$, the integral will receive a substantial contribution from the neighborhood of this point. It is the contention of this paper that, for reasonably well-developed seas, this contribution in fact forms a sufficiently large part of the integral to make possible the estimate

$$K(\omega_1(\Omega_0, 0), 0) + K(\omega_2(\Omega_0, 0), 0) = 2\,K(\omega_0, 0),$$

and hence $F(\omega_0, 0)$ from a knowledge of $G(\Omega_0)$ alone.

This kinematic amplification of the $\boldsymbol{k}_0$ component may be understood physically as follows: In the neighborhood of $\boldsymbol{k}_0$ the apparent frequency of the $\boldsymbol{k}$ component is given approximately by the leading terms of the Taylor-series expansion

$$\Omega(\boldsymbol{k}) = \Omega(\boldsymbol{k}_0) + (\boldsymbol{k} - \boldsymbol{k}_0) \cdot \nabla_{\boldsymbol{k}} \Omega(\boldsymbol{k}_0) + \ldots .$$

But from (4),

$$\nabla_{\boldsymbol{k}} \Omega(\boldsymbol{k}_0) = \boldsymbol{V}(\boldsymbol{k}_0) - \boldsymbol{U} = \boldsymbol{0},$$

so that, correct to first order,

$$\Omega(\boldsymbol{k}) = \Omega(\boldsymbol{k}_0) = \Omega_0 .$$

The kinematic amplification of the $\boldsymbol{k}_0$ component is thus seen to be a consequence of the fact that wave components in the neighborhood of $\boldsymbol{k}_0$ have essentially the same apparent frequency, Ω_0 (cf. Fig. 3). If $F(\boldsymbol{k})$ varies sufficiently slowly in this neighborhood, the resulting value of $G(\Omega_0)$ will have a strong dependence on $F(\boldsymbol{k}_0)$. This dependence is further strengthened by the geometric amplification of the $\boldsymbol{k}_0$ component as a result of the spatial response of the wave recorder, which has an effective beam width of 20 degrees for wave components with the apparent frequency Ω_0.

An index of the strength of the dependence of $G(\Omega_0)$ upon $F(\boldsymbol{k}_0)$, because of the kinematic and geometric amplification of the $\boldsymbol{k}_0$ component, is the insensitivity of the ratio $H = F(\omega_0, 0)/G(\Omega_0)$ to the form of $F(\omega, \vartheta)$. In order to demonstrate this insensitivity, H is plotted in Fig. 4 as a function of $G(\Omega_0)$ for several model spectra of the form

$$F(\omega, \vartheta) = F(\omega)\,D(\vartheta),$$

where

$$D(\vartheta) \equiv \frac{2}{\pi} D_1 \cos^2\vartheta + \frac{8}{3\pi} D_2 \cos^4\vartheta + \frac{16}{5\pi} D_3 \cos^6\vartheta, \; |\vartheta| < \frac{\pi}{2},$$

$$\equiv 0, \; |\vartheta| \geqslant \frac{\pi}{2},$$

and

$$D_1 + D_2 + D_3 = 1 .$$

$F(\omega)$ is given one of three forms.

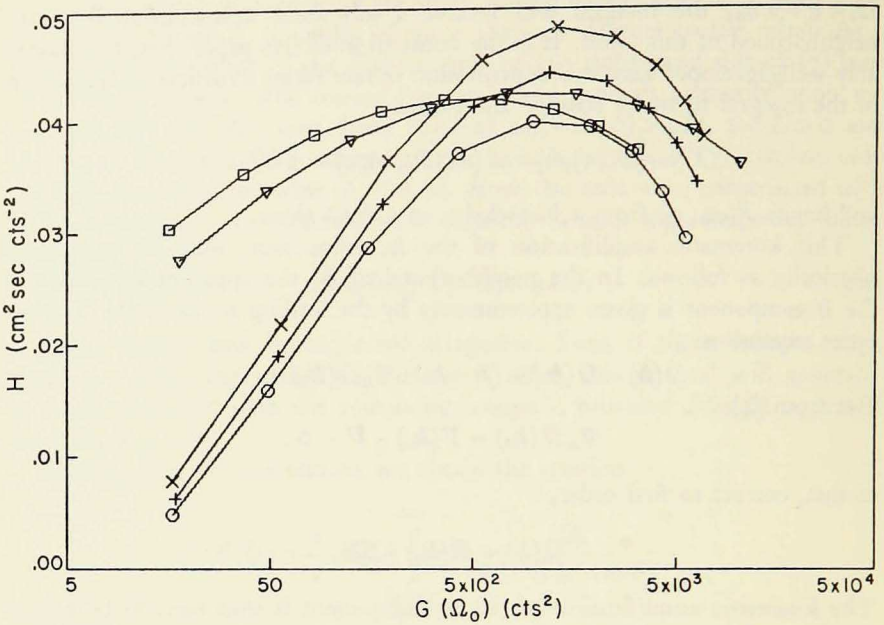

Figure 4. The ratio of $F(\omega_0, o)$ to $G(\Omega_0)$. The units of $G(\Omega_0)$ refer to the counts of a digital recording system. $\times$, standard spectrum, $D_1 = D_2 = o$; $+$, standard spectrum, $D_1 = D_3 = o$; o, standard spectrum, $D_2 = D_3 = o$; $\square$, substandard spectrum, $D_1 = D_3 = o$; $\triangledown$, Neumann spectrum, $D_1 = D_3 = o$.

(i) The Standard Spectrum:

$$F(\omega) = \varepsilon g^2 \omega^{-5} e^{-5/4\,(\omega_m/\omega)^4},$$

where $\varepsilon \equiv 7.4 \times 10^{-3}$. The standard spectrum is essentially the spectrum of Pierson and Moskowitz (1964).[4]

(ii) The Substandard Spectrum:

$$F(\omega) = \varepsilon g^2 \omega^{-5} e^{-5/2\,(\omega_m/\omega)^2}.$$

The substandard spectrum is similar in form to a spectrum proposed by Roll and Fischer (1956), but it is normalized differently. The peak value of the substandard spectrum is only 30% of that of the standard spectrum. The substandard spectrum does not give a good fit to existing data and is introduced only to illustrate the insensitivity of the ratio plot to the form of $F(\omega, \vartheta)$.

We note that both the standard and the substandard spectra have the asymptotic behavior

$$F(\omega) \sim \varepsilon g^2 \omega^{-5}, \text{ for large } \omega,$$

which is Phillips' equilibrium spectrum (1958).

4. These authors find $\varepsilon = 8.1 \times 10^{-3}$.

(iii) The Neumann Spectrum:

$$F(\omega) = \mu \omega^{-6} e^{-3(\omega_m/\omega)^2},$$

where $\mu \equiv 4.8 \times 10^4$ cm^2 sec^{-5}. This spectrum was proposed by Neumann (1954).

It is clear from Fig. 4 that the recovery of $F(\boldsymbol{k}_0)$ will be successful and relatively independent of the spectral model when $G(\Omega_0)$ is sufficiently large. For $G(\Omega_0) > 250$ cts^2, the spread implied by Fig. 4 is $\pm 10\%$.

3.3. *Spectral Analysis.* The spectral analysis of the wave records will be treated in a separate paper and is here summarized only briefly. The analysis is based on a generalization of the analysis of stationary random variables to random variables whose statistical properties vary slowly in time. Such variables are termed quasistationary random variables. In analogy to the energy spectrum of a stationary random variable, we define the local energy spectrum $E(t, \Omega)$ of a quasistationary random variable $f(t)$.

$$E(t,\Omega) \equiv \frac{1}{2\pi} \int_{-\infty}^{\infty} d\tau\, C(t,\tau)\, e^{-i\Omega\tau},$$

where

$$C(t,\tau) \equiv \langle f(t) f(t+\tau) \rangle .$$

The brackets denote an ensemble average. The approximation

$$E(t,\Omega) \simeq \frac{1}{2\pi} \int_{-\infty}^{\infty} d\tau\, C(t,\tau) \cos \Omega\tau$$

and the inverse relation

$$C(t,\tau) \simeq \int_{-\infty}^{\infty} d\Omega\, E(t,\Omega) \cos \Omega\tau$$

involve the neglect of quantities of order $\tau(\partial/\partial t)\, C(t, \tau)$. A smoothed spectrum $G(t, \sigma)$ is defined by a relationship analogous to (12). An estimate of $G(t, \sigma)$ is obtained from a single record of finite length by two different techniques; (i) the method of partical series and (ii) the method of partial spectra. In (i) the record is subdivided into a finite number of subrecords and a time average of $G(t, \sigma)$ is estimated for each subrecord; (i) is the method usually employed in the analysis of quasistationary time series. Method (ii) depends upon an expansion of $G(t, \sigma)$ in orthogonal polynomials in t. The coefficient of the

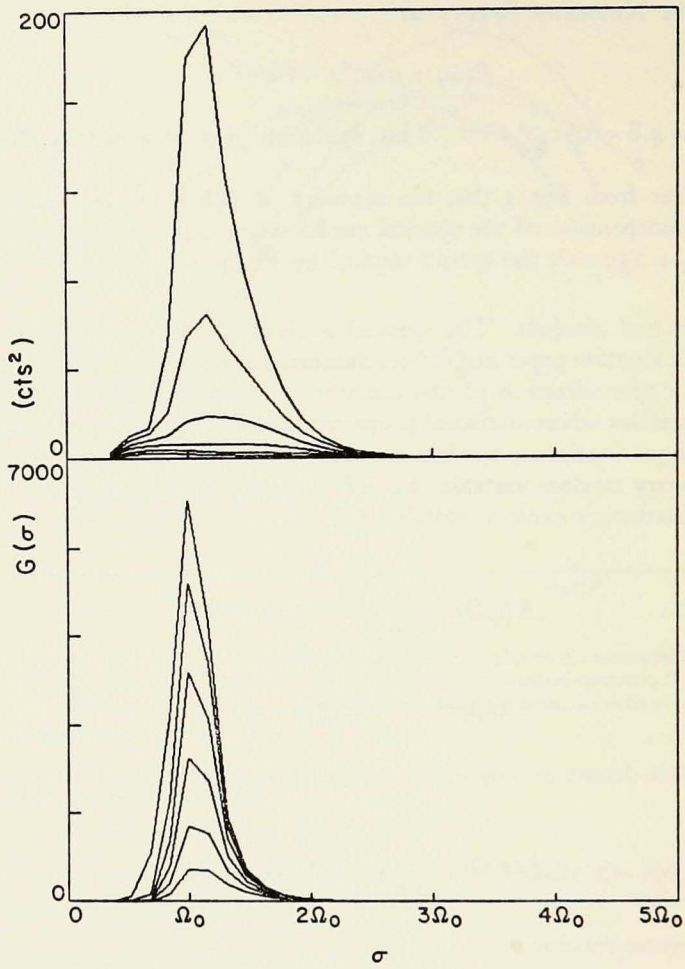

Figure 5. Apparent spectrum computed for the standard spectrum with $D_1 = D_3 = 0$. Spectra are shown for $\omega_m = 1.00, 1.25, \ldots, 3.00$ sec^{-1}.

nth term of the expansion is essentially the cospectrum of the record and the product of the record with the nth-order polynomial.

The partial-series estimates for several representative runs are presented in Appendix A (pp. 173–175). The spectra are plotted at intervals of 0.5×10^3 sec. The 95% confidence limits for these spectra are 0.7 to 1.6. The major feature of the observed spectra is the peak in the neighborhood of $\Omega = \Omega_0$. The location of this peak is expected from the kinematic and geometric amplification of the $\boldsymbol{k}_0$ component. The location and general shape of the peak is consistent with apparent spectra computed from various model spectra (cf. Fig. 5).

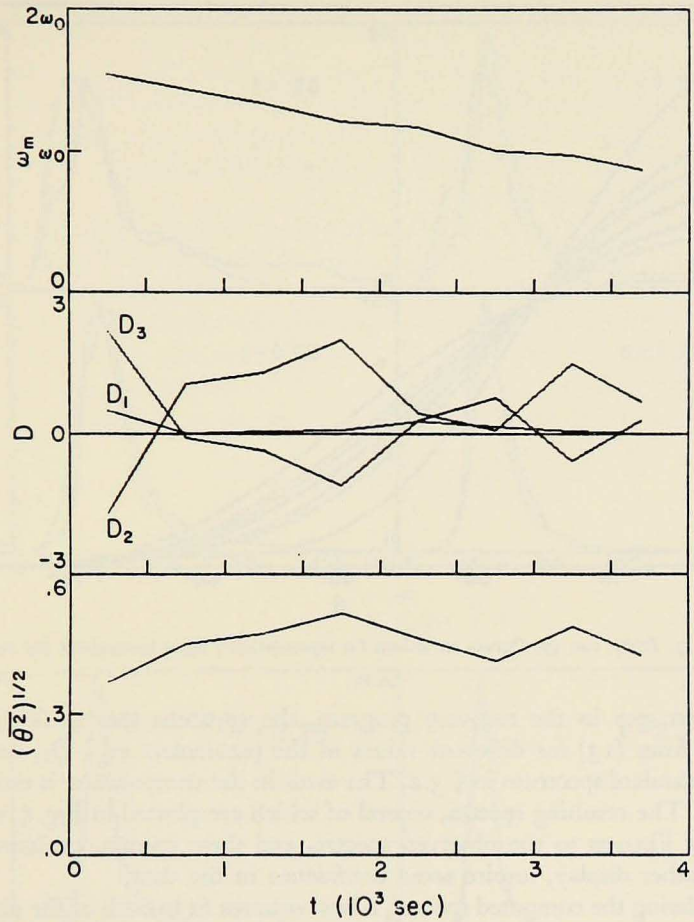

Figure 6. The parameters ω_m, D_1, D_2, D_3, and $(\overline{\vartheta^2})^{1/2}$; run 37.

3.4. *Recovery of the Growth Curves.* One method of recovering $F(\boldsymbol{k}_0)$ from the spectrum $G(\sigma)$ is afforded by the ratio plot. This plot is smoothed, and $F(\omega_0, 0)$ is computed from the relation

$$F(\omega_0, 0) = \overline{H}(G(\Omega_0))\, G(\Omega_0)\,,$$

where $\overline{H}(G)$ is the smoothed plot. The recovery method actually employed was somewhat more sophisticated, though not necessarily more reliable. The basic idea of the method was to use the entire apparent spectrum to get some idea of the general form of $F(\omega, \vartheta)$ and hence to determine the appropriate branch of the ratio plot.

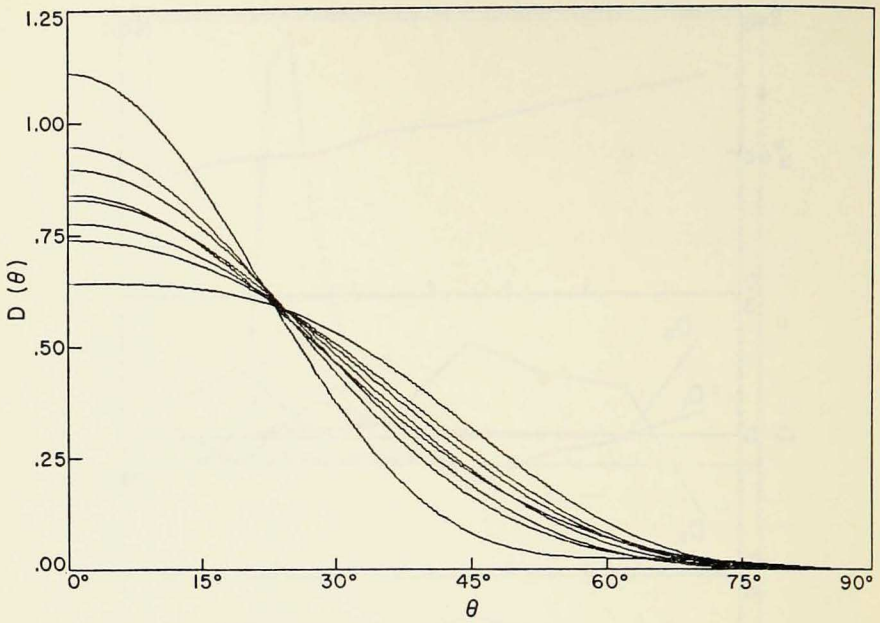

Figure 7. $D(\vartheta)$; run 37. Curves are drawn for representative times throughout the run.

As a first step in the recovery program, the apparent spectra $G(\sigma)$ were computed from (13) for different values of the parameters ω_m, D_2, and D_3, using the standard spectrum in § 3.2. The error in the computation is estimated to be 2%. The resulting spectra, several of which are plotted in Fig. 5, show a remarkable likeness to the observed spectra, and these spectra, perhaps more than any other display, inspire some confidence in the data.

Interpolating the computed spectra, a least-squares fit to each of the observed spectra was determined, and a corresponding value of $F(\omega_0, 0)$ was computed from the minimizing parameters. The resulting fit for run 37 is presented in Figs. 6, 7, and 8. In Fig. 6 the minimizing parameters are plotted as functions of time. The "beam width" $(\overline{\vartheta^2})^{1/2}$ is defined by the relation

$$(\overline{\vartheta^2})^{1/2} \equiv [\int_{-\pi/2}^{\pi/2} d\vartheta\, \vartheta^2 D(\vartheta)]^{1/2}.$$

The corresponding functions $D(\vartheta)$ are plotted in Fig. 7. A comparison of the best-fit spectra and the observed spectra is given in Fig. 8. The fit is seen to improve substantially throughout the course of the run. It is somewhat surprising that the early spectra can be fit at all, since $F(\boldsymbol{k}_0)$ is not significant for these spectra. The apparent spectrum is therefore determined by a range of $\boldsymbol{k}$, and the product form for the model spectrum is clearly a restrictive approximation.

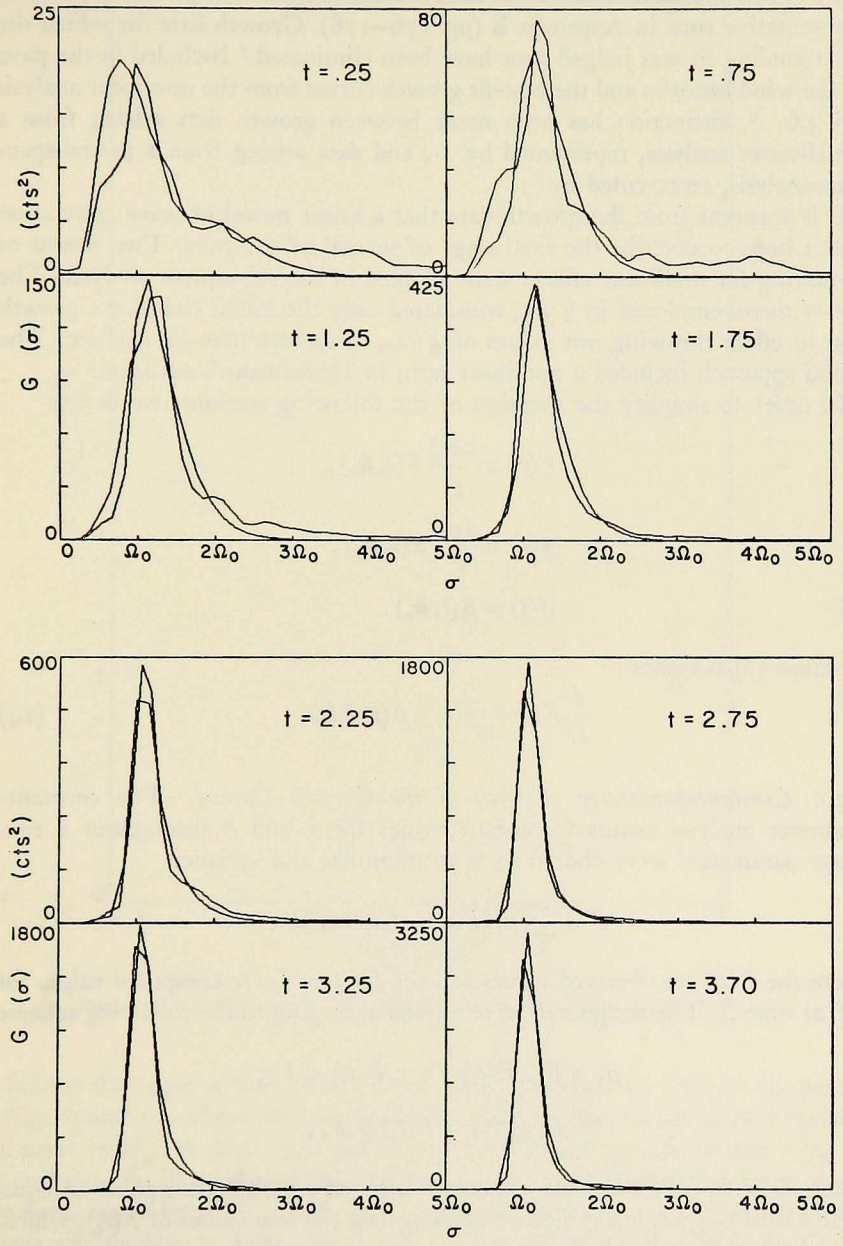

Figure 8. Comparison of the best-fit spectra and the observed spectra; run 37. Times t are in units of 10^3 sec.

The growth data resulting from the recovery program are plotted for several representative runs in Appendix B (pp. 176–178). Growth data for which the corresponding fit was judged poor have been eliminated.[5] Included in the plots are the wind histories and the best-fit growth curves from the nonlinear analysis in § 3.6. A distinction has been made between growth data arising from a partial-series analysis, represented by +, and data arising from a partial-spectrum analysis, represented by □.

It is apparent from the growth data that a linear model of wave generation cannot hope to describe the final stage of several of the runs. Two means of accounting for nonlinear effects were adopted in the subsequent analysis. The first of these, employed in § 3.5, considered only the initial rise of the growth data, in effect throwing out values of $F(\omega_0, 0)$ greater than 80 cm² sec. The second approach included a nonlinear term in Hasselmann's equation.

In order to simplify the notation of the following sections, we define

$$F(t) \equiv \frac{2\omega_0^3}{g^2} F(t, \boldsymbol{k}_0),$$

$$\alpha(t) \equiv \frac{2\omega_0^3}{g^2} \alpha(t, \boldsymbol{k}_0),$$

and

$$\beta(t) \equiv \beta(t, \boldsymbol{k}_0).$$

Equation (2) becomes

$$\frac{d}{dt} F(t) = \alpha(t) + \beta(t) F(t). \tag{14}$$

3.5. *Constant-parameter Analysis of the Growth Curves.* The constant-parameter analysis assumed constant values for α and β throughout a run. These parameters were chosen so as to minimize the variance

$$V \equiv \sum_i \mu_i [F(t_i) - f(t_i, \alpha, \beta)]^2,$$

where the $F(t_i)$ are observed values and the $f(t_i, \alpha, \beta)$ are computed values for $F(t)$ at time t_i. The weights μ_i were chosen according to the following scheme

$$\mu_i \equiv F_0^{-1} F(t_i)^{-1}, \quad F(t_i) \leqslant F_0,$$

$$\equiv F(t_i)^{-2}, \quad F(t_i) > F_0,$$

where $F_0 = 10$ cm² sec. This choice tends to give each datum point an equal proportional weight, but it discriminates against the low values of $F(t_i)$, which, as can be seen from the ratio plot (Fig. 4), are not as reliable as the higher values.

5. The first few growth data from a run were generally eliminated. Data for which $D(\vartheta)$ was peaked at an angle other than zero (usually verified by visual observation) were also eliminated.

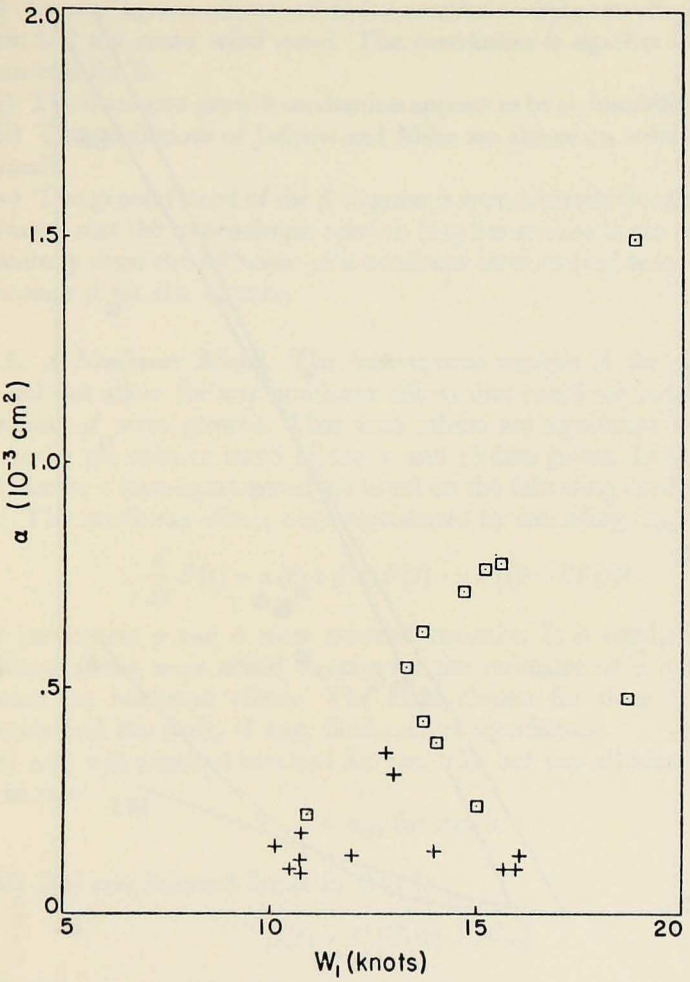

Figure 9. Scatter diagram; α as a function of W_1. Constant-parameter analysis.

Scatter diagrams of the results of the constant-parameter analysis are given in Figs. 9 and 10, where the best-fit values of the parameters are plotted against the mean of W_1. A distinction has been made between runs for which $F(t_i) < 50$ cm^2 sec, for all t_i, represented by +, and runs for which this relation does not hold, represented by □. Included in the diagram for β are: the predicted curves arising from the theories of Jeffreys and Miles, a curve from the fit in § 3.6, and the curve

$$\beta = s(\boldsymbol{k}_0 \cdot \boldsymbol{W} - \omega_0), \tag{15}$$

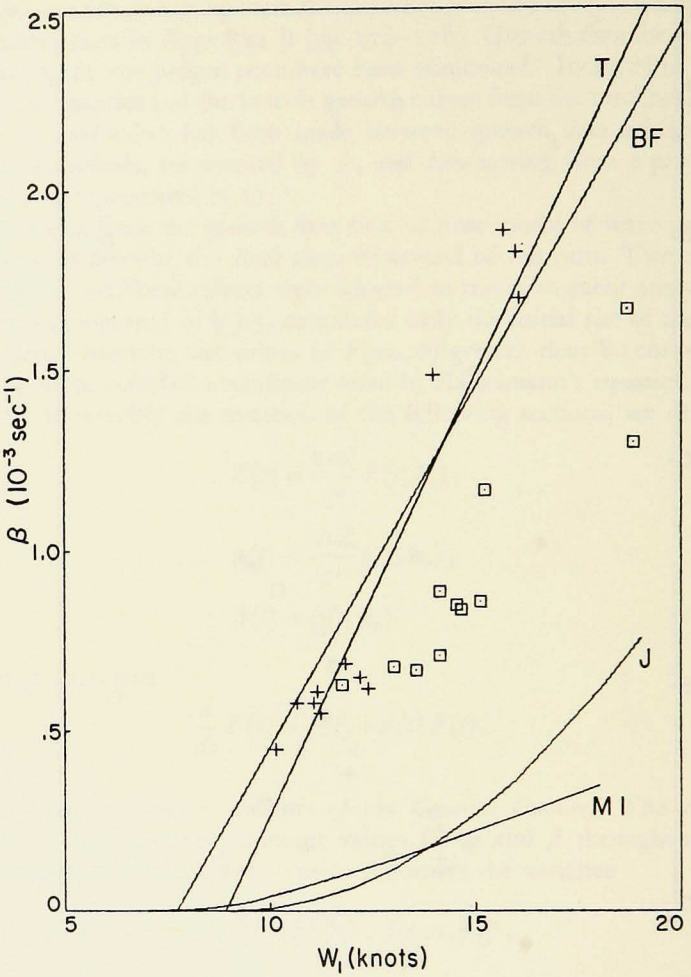

Figure 10. Scatter diagram; β as a function of W_1. Constant-parameter analysis. *J*, Jeffreys (1925); *MI*, Miles (1957); *BF*, best fit in § 3.6; *T*, relation (15).

where W is the mean wind velocity at a critical wave length above the water surface and s is the ratio of the density of air to that of seawater. These relations have been normalized to wind speeds measured at anemometer height on the basis of a logarithmic profile having a roughness length of 0.1 cm. The Jeffreys curve corresponds to a sheltering coefficient of 0.27, the Miles curve to a wind-profile parameter of 3×10^{-3}.

A number of conclusions are already evident from an examination of Figs. 9 and 10.

(i) These diagrams show a definite correlation between the best-fit parameters and the mean wind speed. The correlation is significantly higher for β than it is for α.

(ii) The dominant growth mechanism appears to be an instability mechanism.

(iii) The predictions of Jeffreys and Miles are almost an order of magnitude too small.

(iv) The general trend of the β diagram is approximately linear. It is perhaps significant that the rather simple relation (15) lies as close to the data as it does, particularly since the inclusion of a nonlinear term in (14) would be expected to increase β for the □ runs.

3.6. *A Nonlinear Model.* The least-squares analysis in the preceding section did not allow for any nonlinear effects that could ultimately result in a limitation of wave growth. That such effects are significant is indicated in Fig. 10 by the relative trend of the + and □ data points. In this section we shall discuss a least-squares analysis based on the following nonlinear model.

(i) The nonlinear effects were represented by amending (14) to read

$$\frac{d}{dt}F(t) = \alpha(t) + \beta(t)F(t) - \gamma F(t)^2 - \delta F(t)^3 .$$

The parameters γ and δ were assumed constant. It is emphasized that the nonlinear terms were added to improve the estimates of α and β—not to evaluate the nonlinear effects. The form chosen for these terms is quite arbitrary and has little, if any, fundamental significance.

(ii) $\alpha(t)$ was assumed constant for each run but was allowed to vary from run to run:

$$\alpha = \alpha_n, \text{ for run } n.$$

(iii) $\beta(t)$ was assumed linear in $W_1(t)$:

$$\beta(t) = \lambda[W_1(t) - W_{10}] .$$

(iv) The fit was defined by those parameters—$\alpha_1, \alpha_2, \ldots, \alpha_N, \lambda, W_{10}, \gamma$, and δ—that minimized the variance

$$V = \sum_n \sum_i \mu_{ni}[F(t_{ni}) - f(t_{ni}, P)]^2 ,$$

where P refers to the parameter list. The weights μ_{ni} were chosen in essentially the same way as they were chosen in the constant-parameter analysis.

The minimization was accomplished as follows: For given λ, W_{10}, γ, and δ, V was minimized with respect to the α_n. This minimization was simplified by the fact that V is a sum of positive definite terms, each of which depends upon a single α_n. Thus the minimizing values of α_n are those that separately minimize the component terms. The resulting subminimum was evaluated

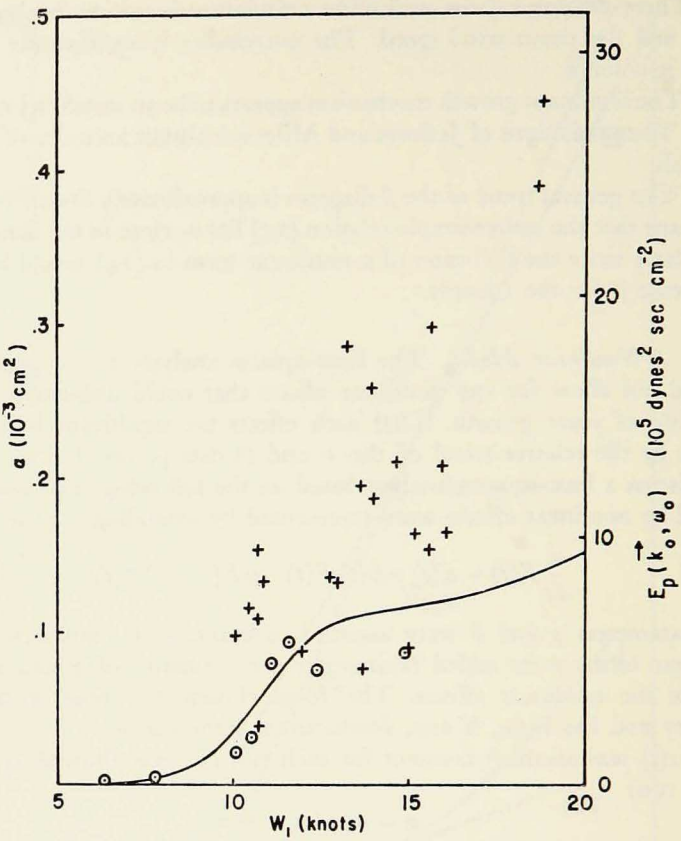

Figure 11. Scatter diagram, α as a function of W_1. Nonlinear analysis. +, Snyder and Cox; ⊙, computed from Phillips' (1957) theory using Priestley's (1965) measurements of atmospheric pressure correlations, and assuming a logarithmic velocity profile with a roughness length of 0.1 cm; —, extrapolation of above computation.

for fixed γ and δ for various values of λ and W_{10}, and the minimizing parameters $\lambda(\gamma, \delta)$ and $W_{10}(\gamma, \delta)$ were determined graphically. It was found that the inclusion of a nonlinear term reduced the minimum variance by a factor of two. The reduction was about the same for a square term ($\delta = 0$) as it was for a cube term ($\gamma = 0$). As the strength of the nonlinear term was increased from zero, the minimum variance decreased rapidly and then rose slowly. For the square term the best fit came for

$$\gamma = 10^{-5}\ \mathrm{cm}^{-2}\ \mathrm{sec}^{-2}. \tag{16}$$

This fit is plotted for several representative runs in Appendix B (pp. 176–178).

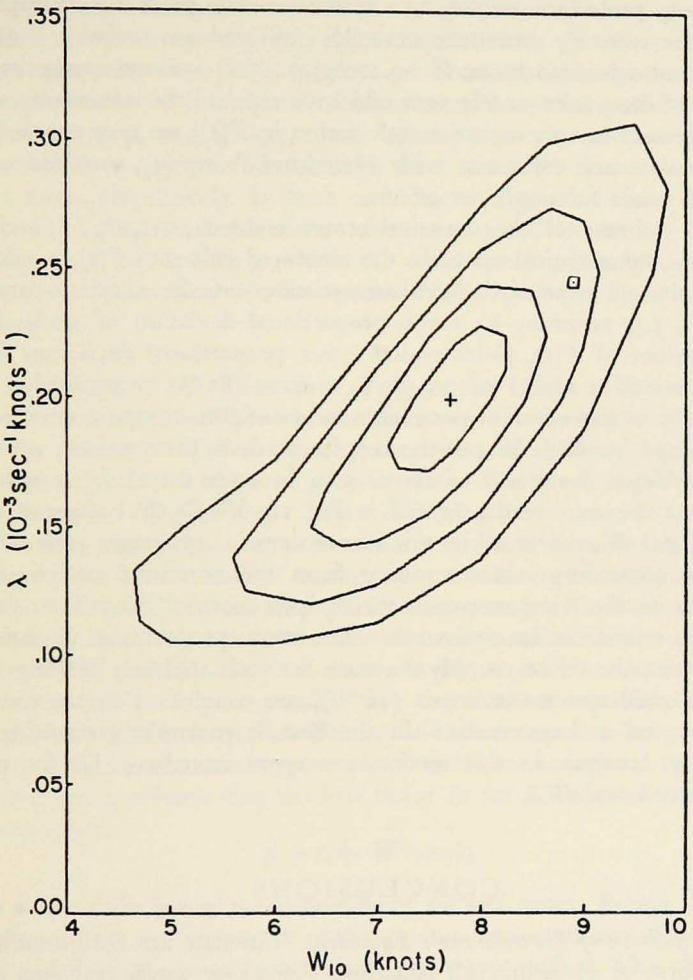

Figure 12. Contour diagram for the variance V. Contours shown are 10%, 30%, 60%, and 100% above the minimum. +, approximate location of the minimum; □, relation(15).

A scatter diagram of the minimizing parameters α_n is given in Fig. 11. A comparison of Fig. 11 with Fig. 9 indicates that the nonlinear analysis has substantially improved the correlation between α and W_1. In fig. 12 the sub-minimum variance is contoured as a function of λ and W_{10} for the case (16). Calculation shows that the minimum variance corresponds to an r.m.s. proportional deviation of 30% in the observed values of $F(t)$. We can account for this proportional deviation roughly as follows: sampling error, 22%; error associated with the recovery program, 10%. These errors are estimated

for a recovery procedure employing a smoothed-ratio plot; the corresponding errors for the recovery procedure actually employed are probably somewhat lower, but not significantly so. If we recognize that a more appropriate representation of the nonlinear effects would have reduced the minimum variance and the necessary r.m.s. proportional deviation in $F(t)$, we may conclude that the present data are consistent with Hasselmann's eq. (1), provided suitable allowance is made for nonlinear effects.

A proper estimate of the statistical errors in $\alpha_1, \alpha_2, \ldots, \alpha_N, \lambda$, and W_{10}, generated by the statistical errors in the recovered values of $F(t)$, would have been difficult and expensive. Such an estimate for the constant-parameter analysis in § 3.5, assuming an r.m.s. proportional deviation of 30 % in the recovered values of $F(t)$, yields typical r.m.s. proportional deviations for the best-fit values of α and β of 20–30 % and 10–15 %, respectively. Using the deviations in the constant-parameter values of β to compute deviations in the slope λ and intercept W_{10} of the best linear fit to these values, we obtain r.m.s. proportional deviations of about 5 % in both λ and W_{10}; note that this fit is not the same as the fit BF in Fig. 10. While the values of $\alpha_1, \alpha_2, \ldots, \alpha_N, \lambda$, and W_{10} obtained in this manner are in some cases quite different from the corresponding values resulting from the nonlinear analysis in this section (because the constant-parameter analysis does not allow for nonlinear effects), it is reasonable to assume that the r.m.s. proportional deviations in these quantities should be roughly the same for both analyses. Making allowance for assorted systematic errors (10 %), we conclude that the combined error—statistical and systematic—in the best-fit parameters resulting from the nonlinear analysis in this section are approximately 40 % for the α_n and 15 % for λ and W_{10}.

CONCLUSIONS

4.1. *Verification of Hasselmann's Equation.* The data are consistent with a nonlinear form of Hasselmann's equation. For 17-m waves traveling downwind, α is of order 10^{-4} cm^2 and is positively correlated with W_1 (measured 6.1 m above the surface) in the range 10–20 knots or 5–10 m sec^{-1}. β is approximately a linear function of W_1 over this same range. This function has a slope of $(0.20 \pm 0.03) \times 10^{-3}$ sec^{-1} knots^{-1} or $(0.40 \pm 0.06) \times 10^{-3}$ m^{-1} and an intercept of (7.7 ± 1.0) knots or (3.9 ± 0.5) m sec^{-1}.

4.2. *Dominance of an Instability Mechanism.* The dominant mechanism in the generation of 17-m waves appears to be an instability mechanism. An index of this dominance is provided by the transition time (cf. Phillips and Katz 1961), $t(\beta) \equiv ln\, 2/\beta$, when $\alpha = \beta F(t(\beta))$; $t(\beta)$ varies from 1.5×10^3 sec at 10 knots to 0.3×10^3 sec at 20 knots.

While β is significant at anemometer wind speeds equal to, and slightly larger than, the phase speed $C(k_0)$, the extrapolation of the linear fit for β to wind velocities below the phase speed is questionable. Several runs for which the average wind speed was equal to, or less than, the phase speed of 10 knots, notably runs 33–34 and 41–42, never developed to the point where $F(\boldsymbol{k}_0)$ could be reliably recovered. The average wind speeds for these runs were 9.6 and 10.2 knots, respectively. In both cases the average wind speed during the second hour of the run was less than the phase speed. In the last two hours of run 73–74–75–76, during which the wind speed gradually decreased to 7 knots, a significant decay in the spectral intensity of the 17-m component was observed.

4.3. *Inadequacy of the Theories of Jeffreys and Miles.* Although an instability mechanism is indicated by the analysis, it is clear from Fig. 10 that neither the theory of Jeffreys (1925) nor that of Miles (1957) is alone adequate to explain the observed growth rates. The level of Jeffreys' curve could be increased by choosing a larger sheltering coefficient; but, as already noted, the data support a linear rather than a quadratic dependence of β upon wind speed. The level of Miles' curve might also be increased by postulating a suitably nonlogarithmic velocity profile. However, it is doubted that any realistic profile could reproduce the observed relationship. Of the assumptions made by Miles, perhaps the most severe is the neglect of the perturbation Reynolds stresses. It is quite possible that the observed instability cannot be explained in terms of a first-order theory, the basic interaction being essentially nonlinear, at least so far as the atmospheric fields are concerned.

It is perhaps significant that the best linear fit for β is approximated by the simple expression

$$\beta = s(\boldsymbol{k}_0 \cdot \boldsymbol{W} - \omega_0),$$

where s is the ratio between the density of air and water, $\boldsymbol{k}_0$ and ω_0 are the propagation vector and frequency of the 17-m component, and $\boldsymbol{W}$ is the wind velocity measured one wave length above the water surface. This relationship is essentially a linear version of Jeffreys' sheltering relationship. It is not known whether this approximate relationship is generally valid or whether it holds only for the 17-m component.

4.4. *Comparison with the Theory of Phillips.* The observed values of α correspond to an incoherent atmospheric pressure spectral intensity (cf. Hasselmann 1960)

$$E_p(\boldsymbol{k}_0, \omega_0) = \frac{\varrho^2 g^3}{2\pi k_0 \omega_0^3} \alpha \sim 6 \times 10^5 \text{ dynes}^2 \text{ sec cm}^{-2}.$$

Until recently it has not been possible to check this value with actual measurements of atmospheric pressure, because the appropriate measurements had not

been made. A recent series of measurements by Priestley (1965) of the longitudinal, lateral, and diagonal correlations of atmospheric pressure over mowed grass, however, confirms the above spectral value and suggests that Phillips' (1957) mechanism can account for the initial excitation of the 17-m component. Let

$$C_p(\boldsymbol{\xi},\tau) \equiv < P(\boldsymbol{x},t)\,P(\boldsymbol{x}+\boldsymbol{\xi},t+\tau) > ,$$

where $P(\boldsymbol{x}, t)$ is the incoherent component of the atmospheric pressure fluctuations at the water surface. Then

$$E_p(\boldsymbol{k},\omega) = \frac{1}{(2\pi)^3}\int_{-\infty}^{\infty} d^2\xi\, d\tau\, C_p(\boldsymbol{\xi},\tau)\cos(\boldsymbol{k}\cdot\boldsymbol{\xi}-\omega\tau).$$

Priestley introduced the spectrum

$$K(\xi,\omega) \equiv \frac{1}{2\pi}\int_{-\infty}^{\infty} d\tau\, C_p(\xi,\tau)\, e^{-i\omega\tau}$$

and found experimentally that $K(\xi, \omega)$ had the approximate form

$$K(\xi,\omega) \cong \Phi(\omega)\, e^{-\mu_1|\xi_1|-\mu_2|\xi_2|}\, e^{-i\varkappa\xi_1},$$

where μ_1, μ_2, $\varkappa$, and $\Phi(\omega)$ were determined by his experiments. $\varkappa$ was related to a convection velocity $\boldsymbol{W}_c$ by $\varkappa = \omega/W_c$. An analysis of one of Priestley's runs suggested that W_c was equal to the wind speed measured at a height of $2\pi/5\,\varkappa$. μ_1 and μ_2 were found to be functions of $\varkappa$, and $\Phi(\omega)$ was found to be of the form

$$\Phi(\omega) = \chi\,\Phi_0(\omega),$$

where $\Phi_0(\omega)$ was a universal function of ω, and χ was a scaling factor. It follows that

$$\begin{aligned} &E_p(\boldsymbol{k}_0,\omega_0) \\ &\cong \frac{1}{(2\pi)^2}\,\Phi(\omega_0)\int_{-\infty}^{\infty} d\xi_1 \int_{-\infty}^{\infty} d\xi_2\, e^{-\mu_1|\xi_1|-\mu_2|\xi_2|}\cos(k_0-\varkappa)\,\xi_1 \\ &\cong \frac{1}{\pi^2}\,\Phi(\omega_0)\,\frac{1}{\mu_2}\,\frac{\mu_1}{(\mu_1^2+(k_0-\varkappa)^2)}. \end{aligned} \tag{17}$$

Evaluating this expression for eight runs reported in Priestley's paper we obtain the points included in Fig. 11. The agreement is seen to be remarkably good. Assuming that the atmospheric turbulence present during Priestley's measurements was comparable to that present during ours, we may conclude that Phillips' theory probably accounts for the initial excitation of the 17-m

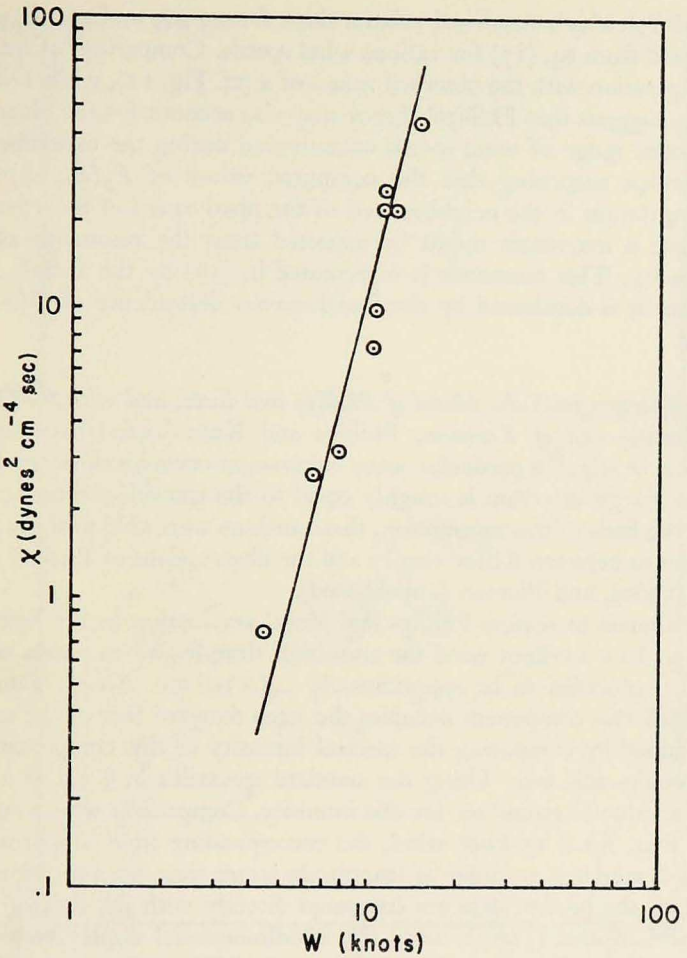

Figure 13. The level of turbulence as a function of wind speed. χ is Priestley's (1965) pressure-spectrum scaling factor. The wind speed W has been normalized to 6.1 m above the water surface, using a logarithmic profile with a roughness length of 0.1 cm. ⊙, Priestley's data. —, best fourth-power fit.

component, at least when the wind speed is in the neighborhood of the phase speed of this component.

Corcos (1964) has shown that, for pipe flow at Reynolds numbers greater than 5×10^4, the root-mean-square pressure at the wall of the pipe is very nearly proportional to the tangential stress. Over water, the tangential stress varies as the square of the wind speed (cf. Van Dorn 1953); thus, the resulting pressure spectrum might be expected to vary as the fourth power of the wind speed. A fourth-power fit to Priestley's data is shown in Fig. 13. Extrapolating

this fit and Priestley's empirical relationships for $\varkappa$, μ_1, and μ_2, $E_p(\boldsymbol{k}_0, \omega_0)$ was computed from eq. (17) for various wind speeds. Comparison of the results of this computation with the observed values of α (cf. Fig. 11), while not totally convincing, suggests that Phillips' theory may also account for the observations over the entire range of wind speeds encountered during the experiments.

It is perhaps surprising that the computed values of $E_p(\boldsymbol{k}_0, \omega_0)$ do not exhibit a maximum in the neighborhood of the phase speed of the 17-m component, since a maximum might be expected from the resonance aspect of Phillips' theory. This resonance is represented in (17) by the factor $\mu_1/(\mu_1^2 + (k+\varkappa)^2)$, but it is dominated by the fourth-power dependence of $\Phi(\omega_0)$ upon wind speed.

4.5. *Comparison with the Model of Phillips and Katz, and with the Observations of Burling and of Kinsman.* Phillips and Katz (1961) have suggested that the time at which a particular wave component occupies the steep forward face of the energy spectrum is roughly equal to the transition time defined in § 4.2. On the basis of this assumption, these authors were able to show a rough correspondence between Miles' theory and the observations of Burling (1955), Kinsman (1960), and Pierson (unpublished).

It is of interest to review Phillips and Katz' assumption in the light of the present data. In a 15-knot wind the transition time for 17-m waves traveling downwind is observed to be approximately 0.5×10^3 sec. An estimate of the time at which this component occupies the steep forward face of the spectrum can be obtained by computing the spectral intensity of this component at the time it occupies this face. Using the standard spectrum in § 3.2 as a model, we obtain a value of 40 cm^2 sec for this intensity. Comparison with runs 45 and 47 shows that, for a 15-knot wind, the corresponding time is approximately 3.5×10^3 sec, which is an order of magnitude larger than the transition time.

In Fig. 14 the present data are compared directly with the data of Burling (1955) and Kinsman (1960), using the nondimensional display employed by Phillips and Katz. In Fig. 14 the wind speeds W have been normalized to one wave length above the water surface, using a logarithmic profile with a roughness length of 0.1 cm. The parameters D, L, and C are respectively the fetch, wave length, and phase speed of that component occupying the inflection point associated with the low-frequency face of the spectrum. Despite some scatter, particularly in Kinsman's data, it is clear that the three sets of data are reasonably consistent, suggesting a universal relationship between the fetch (expressed in wave lengths) at which a wave component occupies the steep forward face of the spectrum and the wind speed (expressed in multiples of the phase speed).

4.6. *Momentum Transfer.* The momentum transfer from wind to water is brought about by both tangential and normal stress. The transfer by tan-

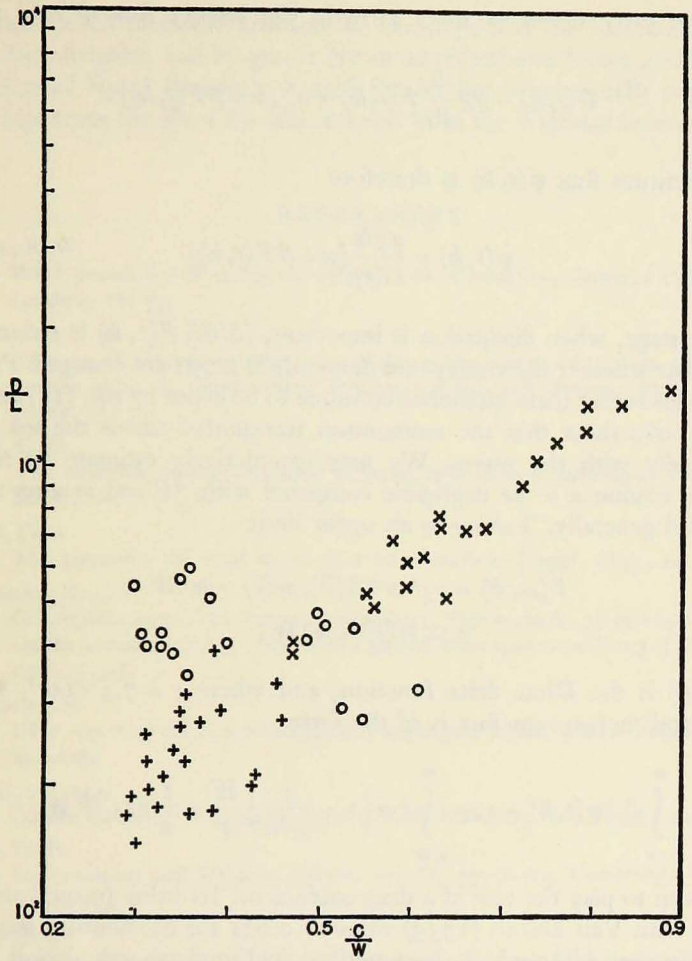

Figure 14. Number of wave lengths before occupation of the steep forward face of the spectrum. +, Burling (1955); o, Kinsman (1960); ×, Snyder and Cox.

gential stress takes place in the absence or presence of waves, while the transfer by normal stress takes place only in the presence of waves. Stewart (1960) has suggested that, in a wind-generated sea, most of the horizontal momentum is in fact transferred by normal stress. This result is borne out by the present series of measurements. Let $\Phi(t, \boldsymbol{k})$ and $\boldsymbol{\psi}(t, \boldsymbol{k})$ be the mean energy and momentum fluxes across the water surface as a result of the interaction of the $\boldsymbol{k}$ component with fluctuations of atmospheric pressure, as determined by an observer moving with the group volocity $\boldsymbol{V}(\boldsymbol{k})$. Then it can be shown that

$$\boldsymbol{\psi}(t, \boldsymbol{k}) = \frac{\boldsymbol{k}}{\omega(k)} \Phi(t, \boldsymbol{k}).$$

During the early stages of wave growth, the energy flux $\Phi(t, \boldsymbol{k})$ will be given by

$$\Phi(t, \boldsymbol{k}) = \varrho g \frac{\partial}{\partial t} F(t, \boldsymbol{k}) = \varrho g [\alpha + \beta F(t, \boldsymbol{k})] . \tag{18}$$

The momentum flux $\boldsymbol{\psi}(t, \boldsymbol{k})$ is therefore

$$\boldsymbol{\psi}(t, \boldsymbol{k}) = \frac{\varrho g \boldsymbol{k}}{\omega(k)} [\alpha + \beta F(t, \boldsymbol{k})]. \tag{19}$$

At a later stage, when dissipation is important, $(\partial/\partial t) F(t, \boldsymbol{k})$ is reduced, but it is not clear whether the energy and momentum fluxes are changed. Probably the best guess is that these quantities continue to be given by eqs. (18) and (19). These remarks show that the momentum transported across the sea surface grows rapidly with the waves. We may speculatively estimate its ultimate value. We assume α to be negligible compared with βF and assume relation (15) to hold generally. Taking as an upper limit

$$\begin{aligned} F(\omega, \vartheta) &= \varepsilon g^2 \omega^{-5} \delta(\vartheta), \omega(k) > \boldsymbol{k} \cdot \boldsymbol{W} \\ &= 0, \omega(k) \leqslant \boldsymbol{k} \cdot \boldsymbol{W}, \end{aligned}$$

where $\delta(\vartheta)$ is the Dirac delta function, and where $\varepsilon = 7.4 \times 10^{-3}$, we find that the total momentum flux is of the form

$$\int_{-\infty}^{\infty} d^2 k \boldsymbol{\psi}(t, \boldsymbol{k}) = \varepsilon s \varrho g \int_{g/W}^{\infty} d\omega \left(1 - \frac{g}{\omega W}\right) \frac{\boldsymbol{W}}{\omega^2} = \frac{1}{2} \varepsilon s \varrho W \boldsymbol{W}.$$

ε is thus seen to play the role of a drag coefficient. Its value (0.007) should be compared with Van Dorn's (1953) value of 0.001 for momentum transfer by tangential stress. Although the assumptions in the above calculation tend to give an overestimate of the momentum transfer by normal stress, it seems likely that, for a fully developed sea, this transfer constitutes the major portion of the total momentum transfer.

ACKNOWLEDGMENTS

The Institute of Marine Science at the University of Miami is thanked for its cooperation during the field experiments, and David Mitchell is thanked for the use of his facilities at Governor's Harbor. Walter Munk and Klaus Hasselmann have made valuable suggestions. Delpha McGowan has spent many hours reading records, and Jimmy Larsen, Norman Larsen, and Jean Filloux assisted in several preliminary experiments. This research has been supported

by a grant-in-aid from the Institute of Geophysics at the University of California, Los Angeles, and by grants NONR 2216(12) and NONR 4008(02) from the Office of Naval Research. Russell Snyder has been partially supported by fellowships from the Ford Foundation and from the National Science Foundation.

REFERENCES

BURLING, R. W.
1955. Wind generation of waves on water. Ph.D. dissertation, Imperial Coll., Univ. of London; 181 pp.

CARTWRIGHT, D. E.
1961. The use of directional spectra in studying the output of a wave recorder on a moving ship. *In* Ocean Wave Spectra, pp. 203–218. Prentice Hall, Inc., New Jersey. 357 pp.

CORCOS, G. M.
1964. The structure of the turbulent pressure field in boundary-layer flows. J. Fluid Mech., *18*: 353–378.

ECKART, CARL
1953. The generation of wind waves on a water surface. J. appl. Phys., *24*: 1485–1494.

HASSELMANN, KLAUS
1960. Grundgleichungen der Seegangsvoraussage. Shiffstechnik, *7*: 191–195.
1963. On the nonlinear energy transfer in a gravity wave spectrum. Part 3. J. Fluid Mech., *15*: 385–398.

HELMHOLTZ, H.
1868. Uber discontinuirliche Flussigkeitsbewegungen. Mber. preuss. Akad. Wiss., pp. 215–228.

JEFFREYS, HAROLD
1925. On the formation of water waves by wind. Proc. roy. Soc., *A107*: 189–206.

KELVIN, W. H.
1910. Mathematical and Physical Papers, vol. IV, pp. 76–85. Cambridge Univ. Press, Cambridge.

KINSMAN, BLAIR
1960. Surface waves at short fetch and low wind speed—a field study. Techn. Rep., Chesapeake Bay Inst., *19*: 169 pp.

MILES, J. W.
1957. On the generation of surface waves by shear flows. Part 1. J. Fluid Mech., *3*: 185–204.

MUNK, WALTER
1955. Wind stress on water: an hypothesis. J. R. meteorol. Soc., *81*: 320–332.

NEUMANN, GERHARD
1954. Zur Charakteristik des Seeganges. Arch. Met., *A7*: 352.

PHILLIPS, O. M.
1957. On the generation of waves by turbulent wind. J. Fluid Mech., *2*: 417–445.
1958. The equilibrium range in the spectrum of wind generated waves. J. Fluid Mech., *4*: 426–434.

PHILLIPS, O. M., and E. J. KATZ
1961. Low frequency components of the spectrum of wind generated waves. J. Mar. Res., *19*: 57–69.

PIERSON, W. J., and L. MOSKOWITZ
1964. A proposed spectral form for fully developed wind seas based on the similarity theory of S. A. Kitaigorodskii. J. geophys. Res., *69*: 5181–5190.

PRIESTLEY, J. T.
1965. Correlation studies of pressure fluctuations on the ground beneath a turbulent boundary layer. Nat. Bur. Stand. Rep., *8942*; 92 pp.

ROLL, H. U., and G. FISCHER
1956. Eine Kritische Bemerkung zum Neumann Spectrum des Seeganges. Dtsch. Hydrogr. Z., *9*: 9–14.

SNYDER, R. L.
1965. The wind generation of ocean waves. Ph.D. dissertation, Univ. of Calif., San Diego; 393 pp.

ST. DENIS, MANLEY, and W. J. PIERSON
1953. On the motions of ships in confused seas. Trans. Soc. Nav. Arch. and Mar. Eng., *61*: 332–357.

STEWART, R. W.
1960. The wave drag of wind over water. J. Fluid Mech., *10*: 189–194.

VAN DORN, W. G.
1953. Wind stress on an artificial pond. J. Mar. Res., *12*: 249–276.

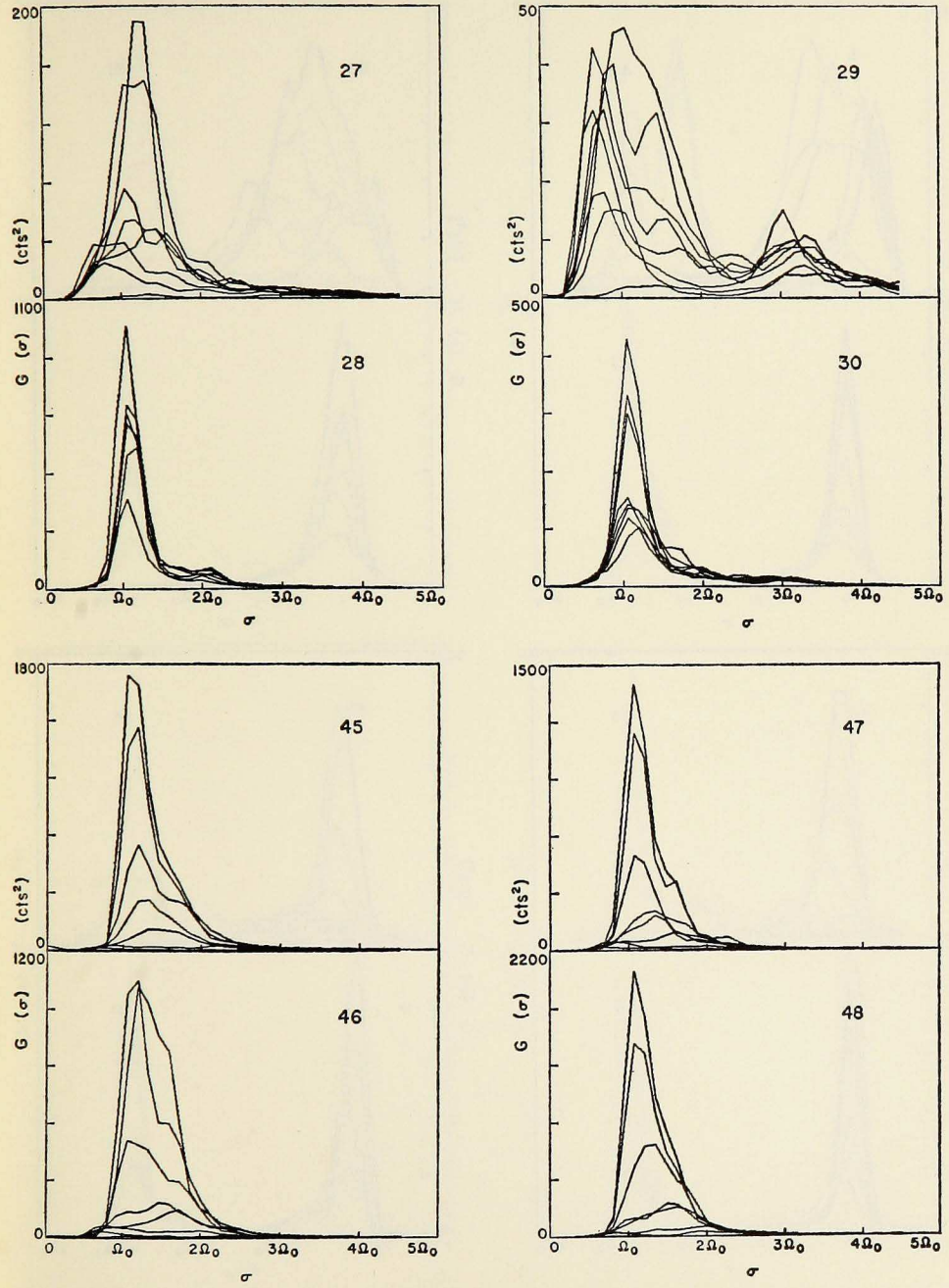

Appendix A. Apparent spectra for selected runs; $G(t, \sigma)$ is given at intervals of 0.5×10^3 sec starting with $t = 0.25 \times 10^3$ sec.

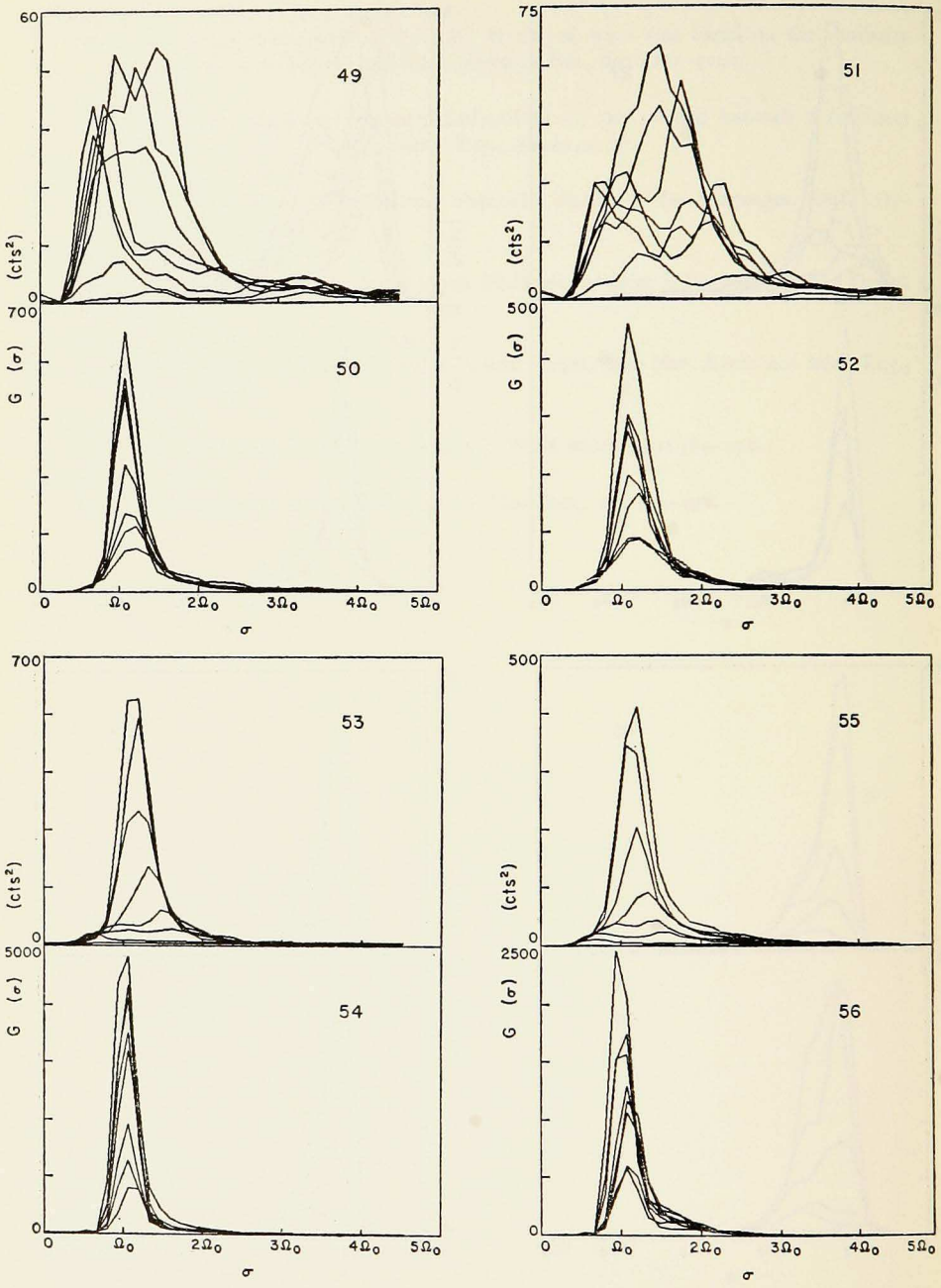

Appendix A. Apparent spectra for selected runs; $G(t, \sigma)$ is given at intervals of 0.5×10^3 sec starting with $t = 0.25 \times 10^3$ sec.

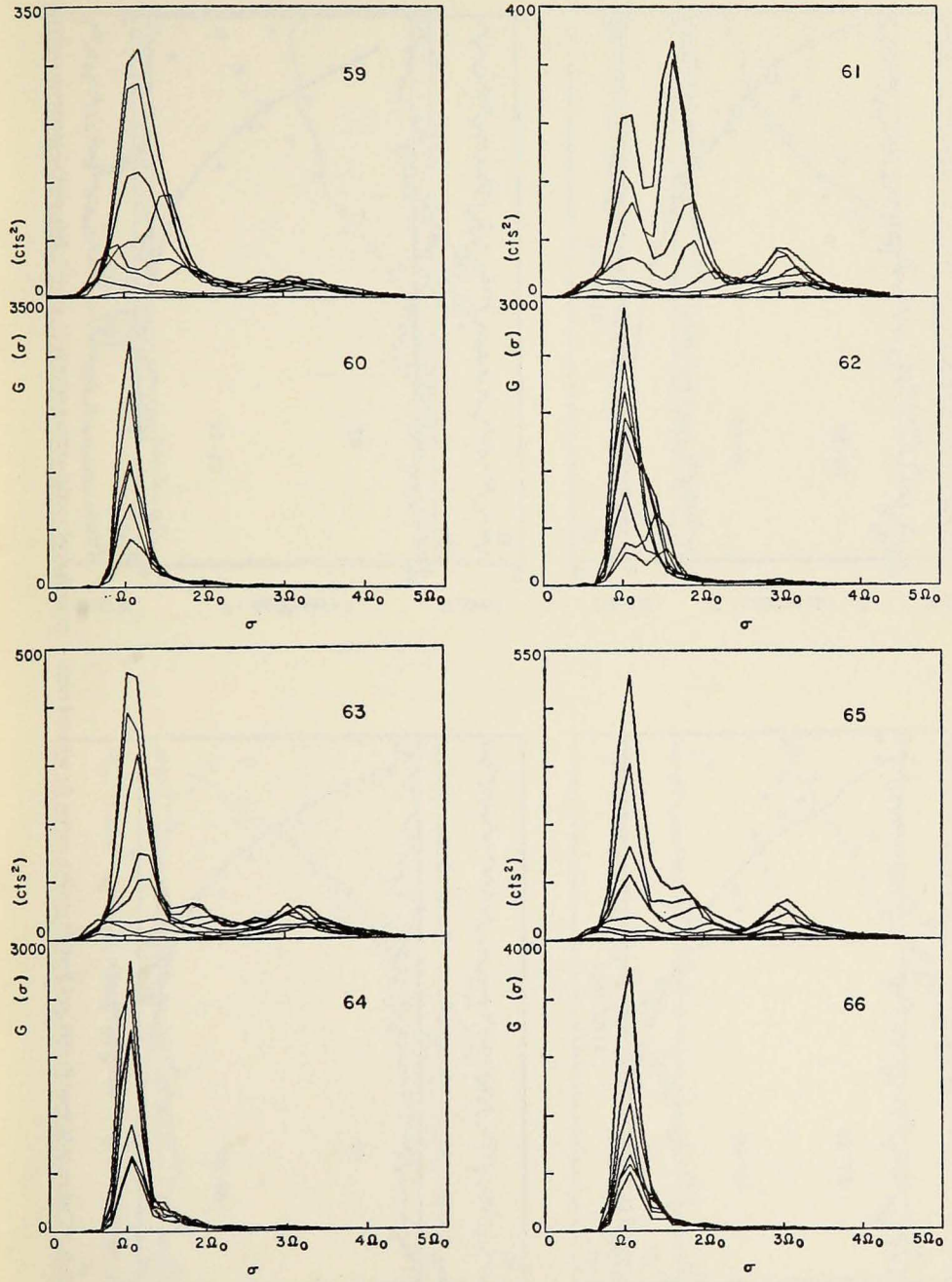

Appendix A. Apparent spectra for selected runs; $G(t, \sigma)$ is given at intervals of 0.5×10^3 sec starting with $t = 0.25 \times 10^3$ sec.

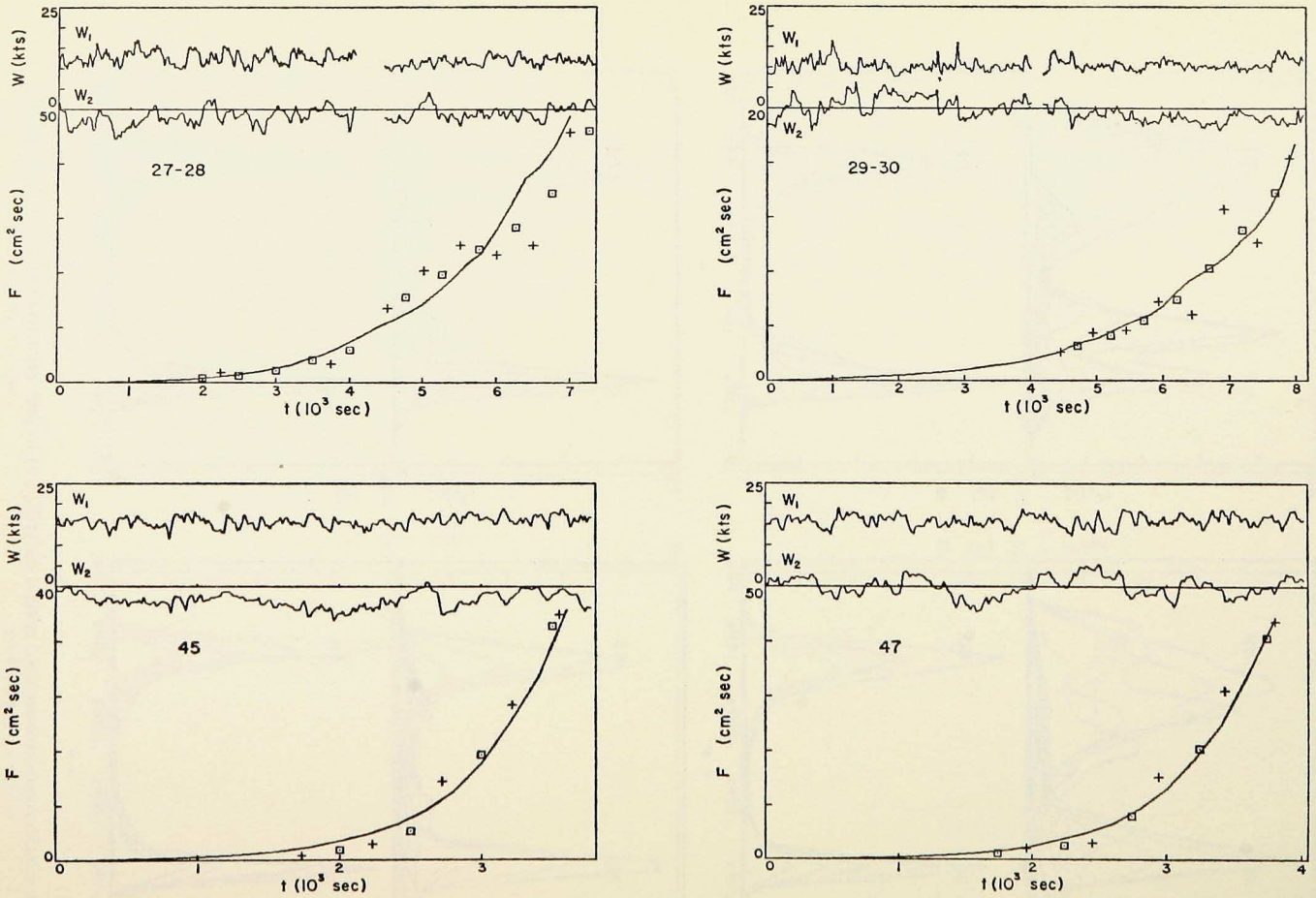

Appendix B. Wind records, growth data, and best-fit growth curves for selected runs. +, growth data, partial-series analysis; □, growth data, partial-spectrum analysis.

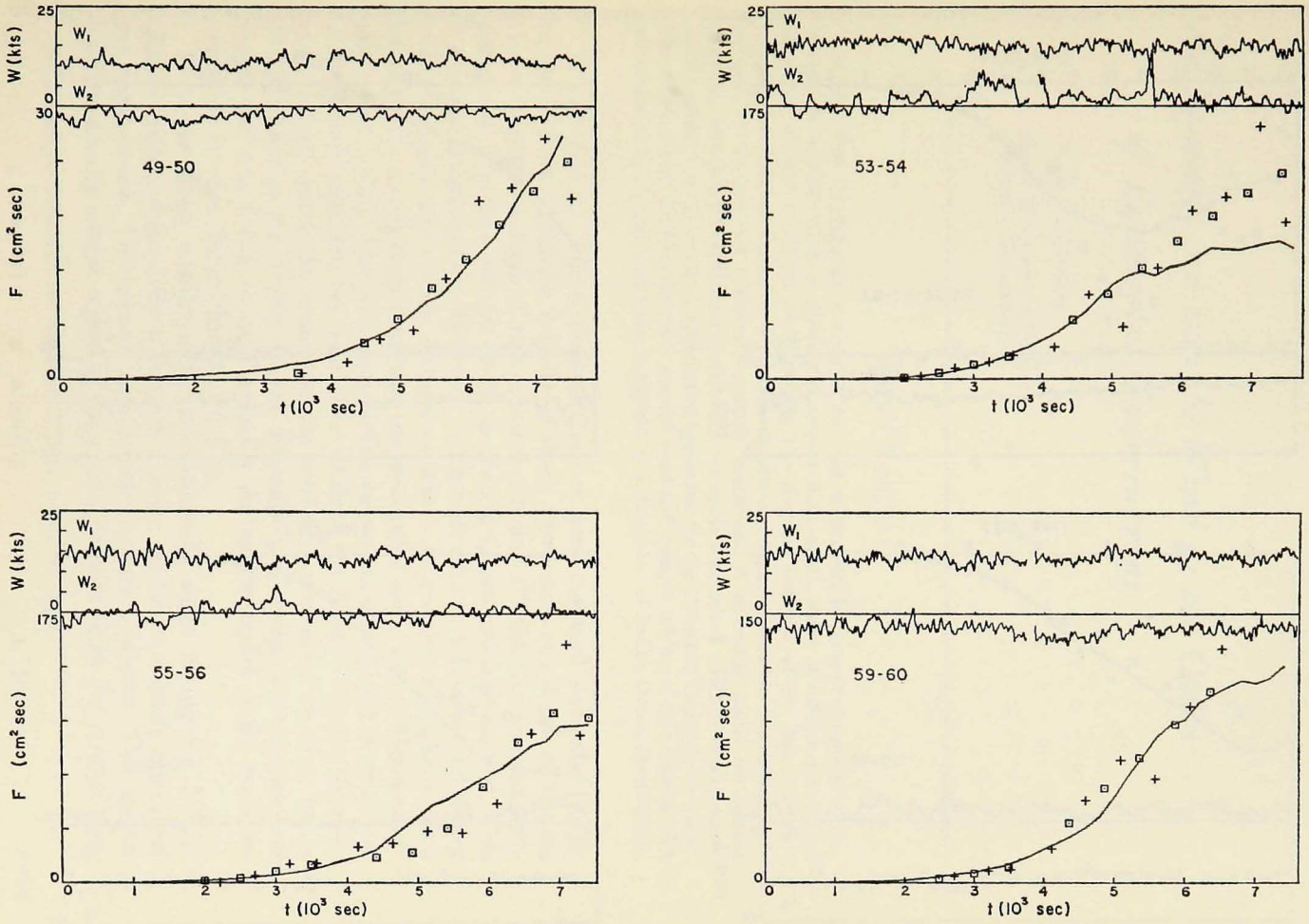

Appendix B. Wind records, growth data, and best-fit growth curves for selected runs. +, growth data, partial-series analysis; □, growth data, partial-spectrum analysis.

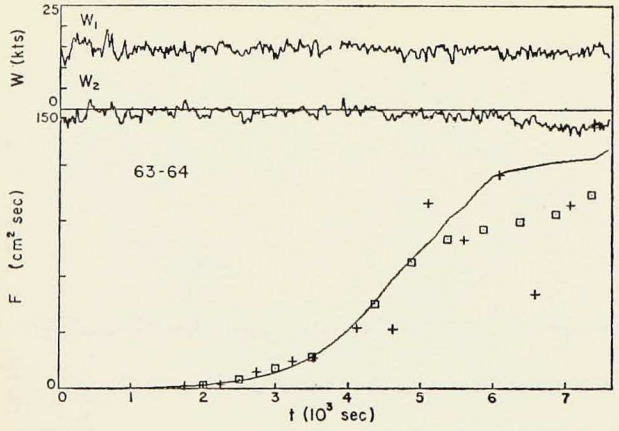

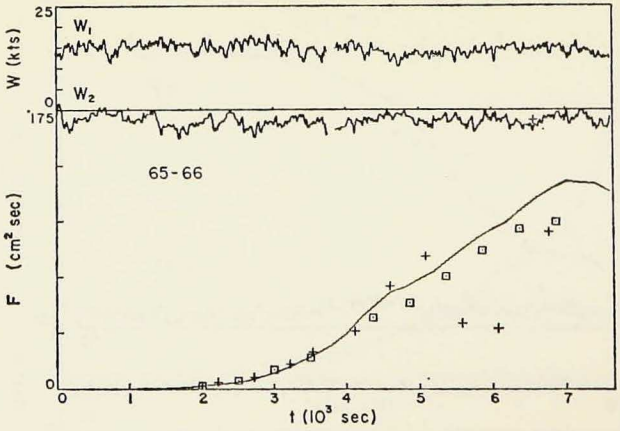

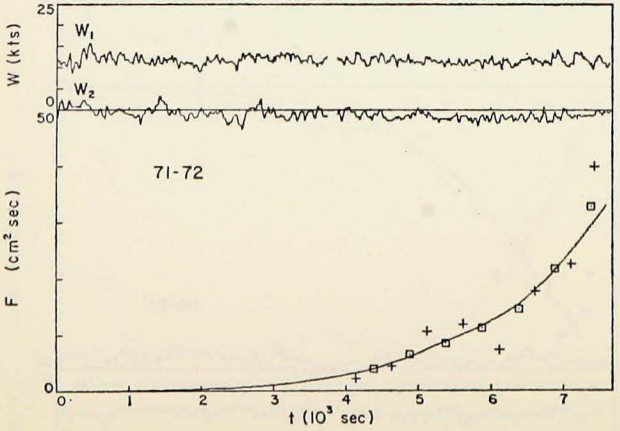

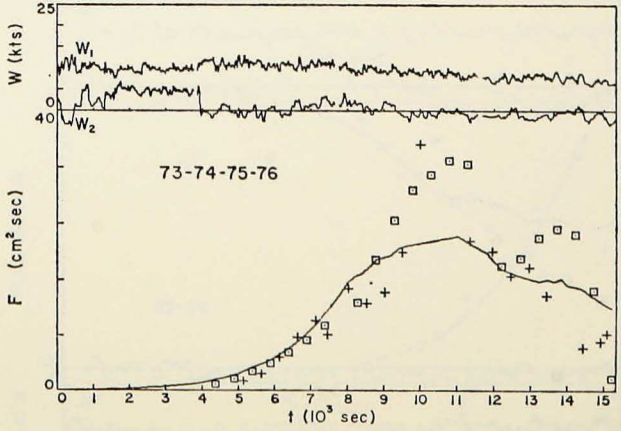

Appendix B. Wind records, growth data, and best-fit growth curves for selected runs. +, growth data, partial-series analysis; □, growth data, partial-spectrum analysis.